

# Surface roughness and three-dimensional heat conduction in thermophysical models



Björn J.R. Davidsson<sup>a,\*</sup>, Hans Rickman<sup>a,b</sup>

<sup>a</sup> Department of Physics and Astronomy, Uppsala University, Box 516, SE-75120 Uppsala, Sweden

<sup>b</sup> PAN Space Research Center, Bartycka 18A, PL-00716 Warsaw, Poland

## ARTICLE INFO

### Article history:

Received 17 April 2014

Revised 22 August 2014

Accepted 22 August 2014

Available online 4 September 2014

### Keywords:

Asteroids, surfaces

Comets, nucleus

Infrared observations

Irregular satellites

Satellites, surfaces

## ABSTRACT

A thermophysical model is presented that considers surface roughness, cast shadows, multiple or single scattering of radiation, visual and thermal infrared self heating, as well as heat conduction in one or three dimensions. The code is suitable for calculating infrared spectral energy distributions for spatially resolved or unresolved minor Solar System bodies without significant atmospheres or sublimation, such as the Moon, Mercury, asteroids, irregular satellites or inactive regions on comet nuclei. It is here used to explore the effects of surface roughness on spatial scales small enough for heat conduction to erase lateral temperature gradients. Analytically derived corrections to one-dimensional models that reproduce the results of three-dimensional modeling are presented. We find that the temperature of terrains with such small-scale roughness is identical to that of smooth surfaces for certain types of topographies and non-scattering material. However, systematic differences between smooth and rough terrains are found for scattering materials, or topographies with prominent positive relief. Contrary to common beliefs, the roughness on small spatial scales may therefore affect the thermal emission of Solar System bodies.

© 2014 Elsevier Inc. All rights reserved.

## 1. Introduction

Early thermal infrared observations of the Moon revealed a significant limb brightening (Pettit and Nicholson, 1930) and unusually slow cooling of certain craters during lunar eclipse (Saari and Shorthill, 1963). Buhl et al. (1968a,b) attributed both phenomena to surface roughness and developed a thermophysical model that reproduced the observations. The model considered surface roughness in the form of concave spherical segments on an otherwise smooth surface, taking into account solar illumination, shadowing, thermal emission, partial re-absorption of scattered or emitted radiation (so-called self heating), and solid state conduction in one dimension. Later, similar crater models have been used to analyze thermal emission from Main Belt Asteroids (e.g., Hansen, 1977; Spencer, 1990; Lagerros, 1996, 1997; Müller and Blommaert, 2004; Delbò and Tanga, 2009), the martian satellites Deimos (Giese and Kühr, 1990) and Phobos (Kühr et al., 1992), planet Mercury (e.g., Emery et al., 1998), Near Earth Asteroids (e.g., Harris et al., 2005; Delbò et al., 2007; Mueller, 2007), and trans-neptunians (e.g., Stansberry et al., 2012). Although spherical segments remain the most common topography in models

accounting for surface roughness, there are alternative approaches like random Gaussian terrains (e.g., Jämsä et al., 1993; Lagerros, 1998; Rozitis and Green, 2011) or cylindrical trenches (e.g. Colwell and Jakosky, 1987; Colwell et al., 1990).

All these authors have assumed that the size scale of topographic features  $D$  is substantially larger than the thermal skin depth  $L$  of the surface material. The thermal skin depth is defined as  $L = \sqrt{\kappa/\rho c \omega}$ , where  $\kappa$ ,  $\rho$  and  $c$  are the heat conductivity, mass density and specific heat capacity, respectively, while  $\omega = 2\pi/\mathcal{P}$  is the angular velocity since  $\mathcal{P}$  is the rotational period of the object under consideration. The surface temperature fluctuates with a certain amplitude during rotation, and  $L$  is formally the depth under the surface at which the amplitude has decreased by a factor  $e \approx 2.7$  with respect to the surface value. Therefore,  $L$  is a measure of the distance over which heat conduction starts to become incapable of transmitting temperature changes from one part of the surface to another. The assumption that  $D \gg L$  is used as a motivation for only considering 1D heat conduction for the smallest resolution elements of the models. Thus, these authors neglect lateral heat conduction and the more advanced models employ a 1D heat equation solver for each facet used in the plate model that resolves the topographic features. However, it is not uncommon that such a detailed consideration of vertical heat conduction within the crater is omitted altogether, and is replaced by various approximate scaling methods. In both cases, strong temperature

\* Corresponding author. Fax: +46 (0)18 4715999.

E-mail addresses: [bjorn.davidsson@physics.uu.se](mailto:bjorn.davidsson@physics.uu.se) (B.J.R. Davidsson), [hans.rickman@physics.uu.se](mailto:hans.rickman@physics.uu.se) (H. Rickman).

gradients arise between shadowed and sunlit parts of the terrains – a property that obviously is needed to reproduce many observed properties of Solar System bodies, such as infrared beaming.

The smallest crater size that safely can be considered with the 1D assumption is on the order of a decimeter for porous regolith, or a meter for compact rock. Roughness on much smaller scales, e.g., due to clumps and clods in regolith or surface texture on rocks, is considered to have no effect on the thermal behavior of the terrain. There are at least two problems with this assumption. Measurements of roughness in high-resolution stereo images of lunar soil acquired by the *Apollo* 11, 12, and 14 crews show that the [Hapke \(1984\)](#) mean slope angle  $\bar{\theta}$  is  $30^\circ \lesssim \bar{\theta} \lesssim 50^\circ$  for  $D \sim 0.1$  mm,  $10^\circ \lesssim \bar{\theta} \lesssim 20^\circ$  for  $D \sim 1$  mm,  $5^\circ \lesssim \bar{\theta} \lesssim 10^\circ$  for  $D \sim 1$  cm, and  $1^\circ \lesssim \bar{\theta} \lesssim 3^\circ$  for  $D \sim 10$  cm ([Helfenstein and Shepard, 1999](#)), noting that  $\bar{\theta}$  increases with the rock versus regolith area coverage ratio. As a comparison, digital terrain models of Asteroid (25143) Itokawa and martian satellite Phobos with spatial resolutions of  $\sim 0.4$  m and  $\sim 27$  m, respectively, both have  $\bar{\theta} \approx 5^\circ$  on average ([Davidsson et al., 2014](#)). This suggests that surface roughness decreases rapidly with increasing  $D$  in the  $10^{-4} \lesssim D \lesssim 1$  m range, and remains quasi-constant at small  $\bar{\theta}$ -values for  $D \gtrsim 1$  m. The level of modeled roughness required to match thermal infrared spectroscopy acquired by the *Lunar Reconnaissance Orbiter* Diviner radiometer corresponds to  $15^\circ \lesssim \bar{\theta} \lesssim 25^\circ$  ([Bandfield et al., 2014](#)). This indicates that the size scale of roughness that most strongly affects the lunar thermal emission is  $D \lesssim 1$  cm, i.e., in a regime where lateral heat conduction may not be negligible.

However, it is not merely the neglect of lateral heat conduction that is problematic. An implicit assumption in most current models is that the thermophysical properties of a piece of terrain of size  $\lesssim L$  approaches those of a mathematically flat surface, in spite of the possible presence of small scale roughness with  $D \ll L$ . The argument is, that if each facet in a plate model (that describes a large crater), in turn would be peppered with small craters, these would become isothermal due to efficient lateral heat conduction within the facet. It is certainly true that temperature gradients are efficiently removed on these small size scales. However, it is not self-evident that the quasi-isothermal surface temperature thus obtained, actually approaches that of a perfectly flat surface.

The purpose of the current paper is to investigate if and when this basic assumption is true, for model terrains with  $14^\circ \lesssim \bar{\theta} \lesssim 39^\circ$ , thus covering the range measured for various Solar System bodies ([Cord et al., 2003](#)). If roughness on small scales has the capacity of elevating or reducing the temperature, with respect to that of a flat surface consisting of the same material, these effects should be quantified. This is done by using a novel thermophysical model of rough terrain that considers 3D heat conduction, in addition to the mechanisms accounted for in the previously mentioned models. The current model has previously been used by [Davidsson et al. \(2013\)](#) to analyze the near-infrared measurements of Comet 9P/Tempel 1 acquired by the spacecraft *Deep Impact* (in that application the code was run in 1D mode, i.e.,  $D \gg L$  was assumed). It has also been used by [Davidsson et al. \(2014\)](#) to investigate the differences and similarities of thermal emission from terrains with identical degree of surface roughness, but different types of topography. The second target of the current paper is to document and describe the model in greater detail than done previously.

The paper is structured as follows. Section 2 contains a detailed documentation of the current model. Section 3 defines basic concepts and provides a motivation for the current study by providing one example of a rough surface with  $D \ll L$  that will be thermally indistinguishable from a flat terrain, and other examples that will differ, according to theory. These theoretical predictions are then verified by numerical computer simulations presented in Section 4. Particularly, we define a criterion that can be used to predict

whether a particular  $D \ll L$  topography will approach the temperature of a similarly illuminated flat surface, or not. We discuss the implications of our study in Section 5.

## 2. A thermophysical model of rough terrains

The thermophysical model consists of different modules for generating topography, defining volumetric grids, calculating self heating, determining solar illumination and shadowing conditions, calculating heat fluxes and temperature versus time and depth, and calculating the emitted spectral energy distribution for resolved or disk-integrated targets, as function of observing geometry. All modules have been implemented in MATLAB, except the thermophysics module that is implemented in FORTRAN. These modules are described individually in the following.

### 2.1. Surface topography

Consider a Cartesian coordinate system  $\{\hat{x}, \hat{y}, \hat{z}\}$ . Topography generation always starts with a quadratic domain in the  $\hat{x}$ – $\hat{y}$ -plane, having control points separated by  $\Delta x$  on the  $\hat{x}$ -axis, and by  $\Delta y = \Delta x$  on the  $\hat{y}$ -axis. Topography is generated by assigning a  $z$ -value to each control point  $\{x, y\}$  on the quadratic mesh, thereby obtaining *surface node points*  $\{x, y, z\}$ . The only limitation is that only *one*  $z$ -value can be assigned to a given control point, preventing the surface from having overhangs.

The four nodes associated with control points  $\{x, y\}$ ,  $\{x + \Delta x, y\}$ ,  $\{x, y + \Delta y\}$ ,  $\{x + \Delta x, y + \Delta y\}$  are used to build two triangles, called *surface facets*. Data matrices are built, that for each facet contain the node position coordinates, outward normal unit vector, and surface area. This information is used to, e.g., calculate surface slope distributions and various parameters that measure the level of surface roughness (see Section 3.2).

Currently supported topographies include concave segments of spheres or ellipsoids with surrounding smooth terrain, random Gaussian surfaces, and parallel sinusoidal trenches, in addition to the flat surface. Nominally, Gaussian surfaces are built by adding a number of randomly placed convex 2D Gaussian functions to an initially flat surface. They therefore consist of a number of peaks elevated above the  $\{\hat{x}, \hat{y}\}$  ground level. We refer to terrains with topography above ground level as *positive relief surfaces*. It is also possible to mirror topographies in the  $\hat{x}$ – $\hat{y}$ -plane, e.g., in order to create *negative relief* random Gaussian surfaces (no topography above the  $\{\hat{x}, \hat{y}\}$  level) or convex spherical segments. Examples of such topographies are shown in Fig. 1.

Surface that locally has positive second  $x$ - and  $y$ -derivatives is here called a *concave* feature, while *convex* features have negative second  $x$ - and  $y$ -derivatives. The positive relief random Gaussian and parallel sinusoidal trench terrains generally contain both convex and concave features, as do negative relief random Gaussian terrains. Since there is no risk of confusion for spherical or ellipsoid segments, they are here referred to as either concave or convex (although negative or positive relief segments are equivalent notations).

### 2.2. Volume elements

The surface topographies described in Section 2.1 are read into a program that adds sub-surface volume down to a pre-defined depth, and divides the 3D domain into a mesh of volume elements or cells. Starting from the bottom of each column corresponding to a square of control points in the  $\hat{x}$ – $\hat{y}$ -plane, cubic elements of height  $\Delta z = \Delta x$  are stacked on top each other as high as possible, i.e., reaching at most the lowest of the four surface nodes above. The remaining volume under the surface is cut along  $\hat{z}$ , through

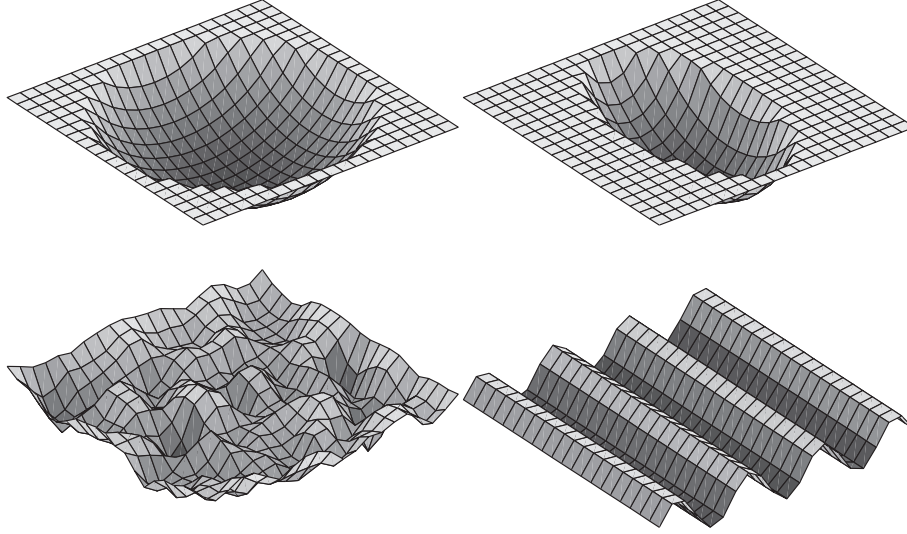


**Fig. 1.** Examples of surface topographies used in thermophysical modeling. Upper left: concave spherical segment on flat surroundings ( $\bar{\theta} = 22.9^\circ$ ,  $s_{rms} = 29.2^\circ$ ,  $\chi = 0.18159$ ,  $\xi = 0.17869$ ). Upper right: concave oblate ellipsoid segment on flat surroundings ( $\bar{\theta} = 22.6^\circ$ ,  $s_{rms} = 26.3^\circ$ ,  $\chi = 0.1796$ ,  $\xi = 0.1747$ ). Lower left: negative relief random Gaussian surface ( $\bar{\theta} = 30.9^\circ$ ,  $s_{rms} = 42.9^\circ$ ,  $\chi = 0.32301$ ,  $\xi = 0.30091$ ). Lower right: parallel sinusoidal trenches ( $\bar{\theta} = 34.3^\circ$ ,  $s_{rms} = 44.2^\circ$ ,  $\chi = 0.24997$ ,  $\xi = 0.30989$ ).

the intersection line of the surface facets, to create two volume elements whose upper surfaces coincide with the facets.

The domain depth and  $\Delta x$ -value need to be selected based on the thermophysical problem to study. The heat conductivity, specific heat capacity, mass density and rotational period are used to calculate the thermal skin depth  $L$ . In order to prevent heat flow across the lower boundary (as assumed during thermophysical calculations, see Section 2.5), the shallowest depth on the domain should be at least  $\sim 7L$ . At the same time,  $L$  should be resolved by at least  $\sim 10$  grid cells to capture temperature gradients sufficiently accurately, which determines  $\Delta x$ . Typically, the code is run with  $\sim 10^3$  surface facets and  $\sim 10^5$  volume elements.

Each volume element is labeled, and all neighbors of every volume element are identified and their labels stored. For each volume element pair in contact, we determine the average distance between the elements (for temperature gradient calculations), as well as their common interface area (for power exchange based on local heat fluxes). For volume elements at the surface, the distance between the surface and the center of the element is used when calculating vertical near-surface temperature gradients. The volume of each cell is calculated since it is needed to convert between internal energy of a cell and its temperature.

### 2.3. Self heating

A given facet  $j$  will generally be illuminated by four types of radiation – direct and diffuse illumination from the Sun, as well as direct and diffuse thermal radiation emitted from the surrounding surface. Diffuse radiation has scattered off another facet  $k$  before arriving at  $j$ . Both types of diffuse illumination and the direct thermal illumination are collectively referred to as *self heating*. Evaluation of the self heating flux at  $j$  requires knowledge of the total flux scattered from or emitted by facet  $k$ , as well as the *fraction* of this flux that actually reaches  $j$ . The first part of the problem can only be dealt with during the actual thermophysical calculation (see Section 2.5) since conditions continuously are changing, but the *fraction* of flux emanating from  $k$  that illuminates  $j$ , called the *view factor*  $\mathcal{F}_{jk}$  is purely geometrical and can be calculated once and for all for a given surface topography.

The view factor for two well-separated facets  $j$  and  $k$  is given by (see, e.g., Özişik, 1985)

$$\mathcal{F}_{jk} = \frac{v_{jk} s_k \cos \theta_j \cos \theta_k}{\pi r^2}, \quad (1)$$

where  $s_k$  is the surface area of facet  $k$ ,  $\theta_j$  and  $\theta_k$  are the angles between the facet outward normals and the line between their centers, and  $r$  is the distance between the facets. Note that  $\mathcal{F}_{jk}$  is set to zero if  $\theta_j \geq 90^\circ$  or  $\theta_k \geq 90^\circ$ . We check if the line of sight between facets  $j$  and  $k$  is intercepted by topography. If so, the visibility switch is  $v_{jk} = 0$ , otherwise  $v_{jk} = 1$ .

Eq. (1) is only valid when  $\sqrt{s_k} \ll r$ . This is not the case for neighboring facets, and  $\mathcal{F}_{jk}$  risks to become unphysically large. Therefore, when  $\mathcal{F}_{jk} > 0.1$ , the facet  $k$  is divided into 130 sub-facets, for which view factors relative to  $j$  are calculated individually and added to a total for  $k$ , that is used to re-define  $\mathcal{F}_{jk}$ . Eq. (1) is derived and discussed at depth in Section 3.1.

Eq. (1) assumes that thermal emission from a locally flat surface is Lambertian. Hapke (1996a,b) solved the coupled radiative transfer and heat conduction equations for a regolith consisting of anisotropically scattering particles. He found that emission is weakly non-Lambertian, only contributing on a  $\sim 20\%$  level to the observed beaming effect of Solar System bodies, primarily being due to hiding of macroscopic cast shadows near opposition. We ignore such smaller local deviations from Lambertian conditions due to particulate medium emission, but do account for the more important angular dependence of thermal emission due to macroscopic topography, illumination and observing geometries (Section 2.6). This introduces a strong deviation from the Lambertian emission law when the surface temperature varies greatly across the terrain. However, for quasi-isothermal surfaces the locally assumed Lambertian function applies globally as well. Hapke also demonstrated that the solid state greenhouse effect may elevate sub-surface temperatures while reducing the surface temperature. Although this effect can become significant for icy particles that are strongly forward-scattering, it is negligible for isotropically scattering grains, such as less transparent regolith particles that are larger than visible wavelengths. It is out of scope in the current model to consider such a sophisticated treatment of energy transfer as that of Hapke (1996a,b), but losses in realism appear small,

and we do consider phenomena that the 1D steady state Hapke model ignored, such as macroscopic surface topography and time-dependence due to body rotation. Furthermore, our model also applies to compact rock, where all regolith-effects disappear.

#### 2.4. Direct solar illumination conditions and shadowing

In order to calculate the direct solar flux for each facet versus time, including the effects of cast shadows, it is necessary to place the terrain with a specific orientation at a certain latitude and longitude on a body that has a particular rotation axis, since this will determine the location of the Sun in the sky as seen from the terrain during rotation. This requires the usage of four right-handed Cartesian coordinate systems with unit principal axes  $\{\mathbf{X}, \mathbf{Y}, \mathbf{Z}\}$  and coordinates  $\{X, Y, Z\}$ , distinguished by the subscripts eq, fs, bf and ss, to be described in the following.

- *The equatorial system (eq)*: the classical system used in astronomy with  $\mathbf{X}_{\text{eq}}$  towards the vernal equinox and  $\mathbf{Z}_{\text{eq}}$  along the positive spin pole of Earth, having its origin coinciding with the body under study.
- *The frame system (fs)*: the  $\mathbf{Z}_{\text{fs}}$ -axis coincides with the positive spin pole of the body. The  $\mathbf{X}_{\text{bf}}$  axis is placed such that the Sun always is located within the  $\mathbf{X}_{\text{fs}}\text{--}\mathbf{Z}_{\text{fs}}$ -plane.
- *The body-fixed system (bf)*: a system that is fixed in the body, coinciding completely with the frame system at rotational phase  $d = 180^\circ$  (corresponding to local noon in the  $\mathbf{X}_{\text{bf}}\text{--}\mathbf{Z}_{\text{bf}}$ -plane) and always having  $\mathbf{Z}_{\text{bf}} = \mathbf{Z}_{\text{fs}}$ . Hence, body rotation is described as rotation of the body-fixed system with respect to the frame system about their common  $\mathbf{Z}$ -axis.
- *The surface system (ss)*: a system fixed in the terrain, identical to the  $\{\hat{x}, \hat{y}, \hat{z}\}$ -system introduced in Section 2.1, but with a specific orientation with respect to the body. The  $\mathbf{X}_{\text{ss}}$ -vector points along a latitudinal line in the direction of body rotation, and the  $\mathbf{Y}_{\text{ss}}$ -vector points along a longitudinal line towards the body north pole. The outward normal  $\mathbf{Z}_{\text{ss}}$  makes an angle  $l_{\text{co}}$  with the body positive spin vector called the *co-latitude*, taking values in the range  $0 \leq l_{\text{co}} \leq 180^\circ$ .

Let the various coordinate systems be defined more stringently through the following transformation matrices. Let the solar unit position vector be  $\hat{\mathbf{S}}_{\odot, \text{eq}} = \{x_{\odot, \text{eq}}, y_{\odot, \text{eq}}, z_{\odot, \text{eq}}\}$  as seen in the equatorial system centered on the body center. In the same system, let  $\hat{\mathbf{P}}_{\text{eq}} = \{\cos \alpha \cos \delta, \sin \alpha \cos \delta, \sin \delta\}$  be the positive spin pole vector of the body, where  $\alpha$  and  $\delta$  are the right ascension and declination of the spin axis, respectively. The coordinate axes of the frame system expressed in equatorial coordinates  $\{\mathbf{X}_{\text{fs,eq}}, \mathbf{Y}_{\text{fs,eq}}, \mathbf{Z}_{\text{fs,eq}}\}$  are then by definition,

$$\begin{cases} \mathbf{Y}_{\text{fs,eq}} = \frac{\hat{\mathbf{P}}_{\text{eq}} \times \hat{\mathbf{S}}_{\odot, \text{eq}}}{|\hat{\mathbf{P}}_{\text{eq}} \times \hat{\mathbf{S}}_{\odot, \text{eq}}|} \\ \mathbf{X}_{\text{fs,eq}} = \frac{\mathbf{Y}_{\text{fs,eq}} \times \hat{\mathbf{P}}_{\text{eq}}}{|\mathbf{Y}_{\text{fs,eq}} \times \hat{\mathbf{P}}_{\text{eq}}|} \\ \mathbf{Z}_{\text{fs,eq}} = \hat{\mathbf{P}}_{\text{eq}} \end{cases} \quad (2)$$

Denote the components of these vectors as  $\mathbf{X}_{\text{fs,eq}} = \{x_1, x_2, x_3\}$  et cetera. A transformation matrix between the frame system and the equatorial system is then obtained as,

$$M_{\text{fs} \rightarrow \text{eq}} = \begin{pmatrix} x_1 & y_1 & z_1 \\ x_2 & y_2 & z_2 \\ x_3 & y_3 & z_3 \end{pmatrix} \quad (3)$$

The transformation matrix between the equatorial system and the frame system is  $M_{\text{eq} \rightarrow \text{fs}} = M_{\text{fs} \rightarrow \text{eq}}^{-1}$ . The transformation matrix between the frame system and the body-fixed system is given by

$$M_{\text{fs} \rightarrow \text{bf}} = \begin{pmatrix} -\cos d & -\sin d & 0 \\ \sin d & -\cos d & 0 \\ 0 & 0 & 1 \end{pmatrix} \quad (4)$$

while the transformation matrix between the body-fixed system and the frame system is  $M_{\text{bf} \rightarrow \text{fs}} = M_{\text{fs} \rightarrow \text{bf}}^{-1}$ . Here,  $d$  is the rotational phase, taking the value  $d = 0$  at local midnight, and increasing towards  $d = 180^\circ$  at local noon, or towards  $d = 360^\circ$  at the following midnight. It is trivially related to the local time  $t$  as

$$d = \frac{360^\circ t}{\mathcal{P}}, \quad (5)$$

where  $\mathcal{P}$  is the rotational period.

Finally, if the terrain under consideration is located at co-latitude  $l_{\text{co}}$ , the transformation matrix between the body-fixed system and the surface system is given by,

$$M_{\text{bf} \rightarrow \text{ss}} = \begin{pmatrix} 0 & 1 & 0 \\ -\cos l_{\text{co}} & 0 & \sin l_{\text{co}} \\ \sin l_{\text{co}} & 0 & \cos l_{\text{co}} \end{pmatrix} \quad (6)$$

and the transformation matrix between the surface system and the body-fixed system is given by  $M_{\text{ss} \rightarrow \text{bf}} = M_{\text{bf} \rightarrow \text{ss}}^{-1}$ .

Therefore, the position vector of the Sun at a rotational phase  $d$ , seen from a terrain at co-latitude  $l_{\text{co}}$ , expressed in the surface system is given by

$$\hat{\mathbf{S}}_{\odot, \text{ss}} = M_{\text{bf} \rightarrow \text{ss}}(l_{\text{co}}) \left( M_{\text{fs} \rightarrow \text{bf}}(d) \left( M_{\text{eq} \rightarrow \text{fs}} \hat{\mathbf{S}}_{\odot, \text{eq}} \right) \right) \quad (7)$$

Given  $\hat{\mathbf{S}}_{\odot, \text{eq}}$ ,  $\{\alpha, \delta\}$ ,  $\mathcal{P}$ ,  $l_{\text{co}}$  and  $d = d(t)$  it is therefore possible to calculate the position of the Sun in the surface system. If the Sun is above the horizon (the angle between  $\hat{\mathbf{S}}_{\odot, \text{ss}}$  and  $\mathbf{Z}_{\text{ss}}$  is below  $90^\circ$ ), and if a particular facet  $j$  is turned towards the Sun (the angle between  $\hat{\mathbf{S}}_{\odot, \text{ss}}$  and the facet normal  $\hat{\mathbf{n}}_j$  is below  $90^\circ$ ), it is necessary to investigate if facet  $j$  has a clear view of the Sun. This is done node by node for each facet  $j$ . If all three nodes of  $j$  have a clear view of the Sun, then the visibility parameter is  $v_{j\odot} = 1$ . If only one node is blocked, then  $v_{j\odot} = 2/3$ . If two nodes are blocked, then  $v_{j\odot} = 1/3$ , and if all nodes of  $j$  are prevented from seeing the Sun, then  $v_{j\odot} = 0$ . The direct solar flux that is absorbed by facet  $j$  is then given by

$$U_j = \frac{S_{\odot}(1-A)v_{j\odot}\hat{\mathbf{S}}_{\odot, \text{ss}} \cdot \hat{\mathbf{n}}_j}{r_h^2} = \frac{S_{\odot}(1-A)v_{j\odot}\mu_j}{r_h^2} \quad (8)$$

where  $S_{\odot}$  is the solar constant,  $A$  is the Bond albedo,  $r_h$  is the heliocentric distance, and  $\mu_j$  is the cosine of the solar incidence angle as seen from facet  $j$ .

Eq. (8) is evaluated for all facets  $j$  for a set of discrete rotational phases  $d$ , typically in steps of  $2^\circ$ . During the thermophysical calculations, the direct solar flux at an arbitrary  $d = d(t)$  is obtained by interpolation of the pre-calculated  $U_j = U_j(d)$  function.

Once the direct solar fluxes  $U_j = U_j(d)$  have been calculated, it is also possible to calculate the diffuse solar radiation fluxes  $W_j = W_j(d)$  once and for all. The code can be run in a single-scattering approximation mode, or in a full multiple-scattering mode. In the single-scattering mode, the fraction of the direct solar radiation that is scattered off a facet  $k$ , and that reaches another facet  $j$ , is assumed to be completely absorbed there. Such an assumption is accurate when  $A \approx 0$ , since little radiation is scattered in the first place. In this case, the diffuse flux is given by

$$W_j = \sum_{k \neq j} \frac{N_{\text{fac}} S_{\odot} A v_{k\odot} \mu_k \mathcal{F}_{jk}}{r_h^2}, \quad (9)$$

where  $N_{\text{fac}}$  is the number of facets. The total solar flux is therefore  $U_j + W_j$ .



However, for higher Bond albedos, it is necessary to consider multiple-scattering while allowing for gradual absorption and loss of scattered radiation to space. This is done through an iterative process,

$$\begin{cases} \mathcal{W}_j^{(0)} = \sum_{k \neq j} \frac{S_{\odot} A v_{k\odot} \mu_k \mathcal{F}_{jk}}{r_h^2} \\ \mathcal{W}_j^{(t+1)} = \sum_{k \neq j}^{N_{\text{fac}}} A \mathcal{W}_k^{(t)} \mathcal{F}_{jk} \\ W_j = \sum_{i=0}^{N_{\text{ms}}} (1-A) \mathcal{W}_j^{(i)} \end{cases} \quad (10)$$

where  $\mathcal{W}_j^{(i)}$  is the flux that illuminates facet  $j$  during step  $i$  in the iteration. The iteration is terminated after  $N_{\text{ms}}$  steps, when the remaining radiation per facet (i.e., the amount of radiation that has not yet escaped or been absorbed) is below a threshold  $\mathcal{W}_{\text{lim}}$

$$\frac{\sum_{j=1}^{N_{\text{fac}}} \mathcal{W}_j^{(N_{\text{ms}})}}{N_{\text{fac}}} < \mathcal{W}_{\text{lim}}, \quad (11)$$

where, typically,  $\mathcal{W}_{\text{lim}} = 10^{-3} \text{ J m}^{-2} \text{ s}^{-1}$ .

## 2.5. Surface and sub-surface temperature

The main computer program reads the data files that describe the geometrical properties of the surface and the sub-surface domain, as well as the illumination conditions (see Sections 2.1, 2.2, 2.3, 2.4), sets initial temperature conditions, and calculates how the temperature changes as function of time and position within the domain during rotation.

Each volume element  $j$  is characterized by a temperature  $T_j$  and an internal energy  $\mathcal{E}_j$ , related by

$$\mathcal{E}_j = \rho c V_j T_j, \quad (12)$$

where the mass density  $\rho$  and the specific heat capacity  $c$  are constants and  $V_j$  is the volume of the element. A surface facet  $j$  is characterized by the surface temperature  $T_{sj}$  that generally is different from the temperature of the underlying volume element.

Given the surface temperatures  $T_{sj} = T_{sj}(t)$  valid at a certain time  $t$ , it is possible to calculate the self heating due to direct and indirect thermal radiation. In the single-scattering mode, the direct thermal self heating flux is given by

$$u_j = \sum_{k \neq j}^{N_{\text{fac}}} \varepsilon \sigma T_{s,k}^4 \mathcal{F}_{jk} \quad (13)$$

where  $\varepsilon$  is the emissivity and  $\sigma$  is the Stefan–Boltzmann constant. The diffuse thermal self heating flux in this mode is  $w_j = 0$  (i.e., apart from the fraction that reaches space, the thermally emitted radiation is re-absorbed completely upon first contact with the surface). In the multiple-scattering mode, the direct thermal self heating flux is instead given by

$$u_j = (1-A) \sum_{k \neq j}^{N_{\text{fac}}} \varepsilon \sigma T_{s,k}^4 \mathcal{F}_{jk} \quad (14)$$

while the diffuse thermal self heating flux is calculated iteratively,

$$\begin{cases} \mathcal{W}_j^{(0)} = \sum_{k \neq j}^{N_{\text{fac}}} \varepsilon \sigma T_{s,k}^4 \mathcal{F}_{jk} \\ \mathcal{W}_j^{(t+1)} = \sum_{k \neq j}^{N_{\text{fac}}} A \mathcal{W}_k^{(t)} \mathcal{F}_{jk} \\ w_j = \sum_{i=1}^{N_{\text{ms}}} (1-A) \mathcal{W}_j^{(i)}. \end{cases} \quad (15)$$

The break criterion is similar to that of Eq. (11).

The code starts with initial conditions  $T_{sj} = T_j = T_0$  for  $\forall j$ ,  $j$  at  $t = 0$ , and calculates modifications to the temperature during gradual time increments  $\Delta t$ . The first task when a time step has been taken is to calculate new surface temperatures. This is done by setting up the surface boundary condition,

$$\begin{aligned} U_j(t) + W_j(t) + u_j(t - \Delta t) + w_j(t - \Delta t) - \varepsilon \sigma T_{sj}^4(t) \\ = \kappa \frac{T_{sj}(t) - T_j(t - \Delta t)}{\Delta z_j}, \end{aligned} \quad (16)$$

where  $\kappa$  is the heat conductivity and  $\Delta z_j$  is the distance between the surface and the center of volume element  $j$ . The first four terms on the left hand side are the absorbed fluxes (direct solar radiation  $U_j$ , diffuse solar radiation  $W_j$ , direct thermal radiation  $u_j$  and diffuse thermal radiation  $w_j$ ).  $U_j + W_j$  are obtained by interpolation of the pre-calculated functions described in Section 2.4. The evaluations of  $u_j$  and  $w_j$  are based on the last known surface temperatures (that are outdated by  $\Delta t$ ). The last term on the left hand side is the emitted thermal radiation. The difference between absorbed and emitted fluxes is balanced by a conductive heat flux, specified on the right hand side. Eq. (16) has the unknown surface temperature of the current time step  $T_{sj}(t)$  in the thermal radiation loss term and in the temperature gradient of the conductive term. It is calculated by solving Eq. (16) using the Newton–Raphson method. An option exists to refine the solution iteratively by replacing  $T_{sj}(t - \Delta t)$  with the newly calculated  $T_{sj}(t)$  and applying the Newton–Raphson method anew. However, tests show that iteration has a negligible effect on the solution when  $\Delta t$  is small, and is typically avoided.

Next, the heat flow between volume elements during  $\Delta t$  is accounted for. The energy exchange between two volume elements  $j$  and  $l$  are calculated by using the Fourier law,

$$\Delta \mathcal{E}_j = \kappa \frac{T_j - T_l}{r_{jl}} a_{jl} \Delta t, \quad (17)$$

where  $r_{jl}$  is the distance between the elements, and  $a_{jl}$  is their common contact area. The internal energy of the volume elements are updated according to  $\mathcal{E}_j(t) = \mathcal{E}_j(t - \Delta t) + \Delta \mathcal{E}_j$  and  $\mathcal{E}_l(t) = \mathcal{E}_l(t - \Delta t) - \Delta \mathcal{E}_j$ , respectively. This is done for each volume element that  $j$  is in contact with. This includes energy transfer between the surface and the interior of the uppermost volume elements, where  $T_l$  in the gradient of Eq. (17) is replaced by  $T_{sj}$ ,  $a_{jl} = s_j$ , and  $r_{jl}$  is replaced by the distance between the surface and the volume element center. No energy is considered to flow across the floor or wall boundaries of the domain, i.e., zero temperature gradients are used as boundary conditions everywhere except for the surface. The floor boundary condition ignores potential heat flow to or from the deep interior due to large-scale seasonal effects caused by motion on an eccentric orbit. However, modeling the entire body down to the core is not a feasible alternative, and the current boundary condition is a reasonable compromise between energy outflow from the considered domain on the inbound leg of the orbit and energy inflow on the outbound leg. Once the net gain or loss of energy from a volume element has been calculated, the new temperature is calculated from Eq. (12).

We therefore do not formulate the energy conservation equation, and do not apply a numerical scheme such as the finite difference method, or the finite element method, in order to solve that equation. Instead, we model the underlying heat flux physics that results in the energy conservation equation. By doing so, we gain simplicity and flexibility – the code was rather straight-forward to implement, and it is relatively easy to add new features when necessary. We do sacrifice speed, since our approach requires the usage of a small time step  $\Delta t$  (typically a few seconds) to obtain stable solutions – but with modern high-speed computers, this is

an attractive alternative to more complex numerical schemes, such as the Crank–Nicolson finite difference method.

The code can be run in 1D or 3D configuration. The 1D case only considers *vertical* heat flow, i.e., changes to the energy  $\mathcal{E}_j$  are only allowed due to heat flow along  $\mathbf{Z}_{ss}$ . The 3D case allows a cell  $j$  to communicate with *all* cells surrounding it, therefore also including *lateral* heat flow. The current implementation of the code only supports constant values of  $\kappa$  and  $c$ , although it could be extended to include temperature-dependent heat conductivity and specific heat capacity rather easily. Implementation of  $\kappa = \kappa(T_j, T_l)$  (potentially using different functions along the three principal directions) is straight-forward. However, conversion between internal energy and temperature becomes somewhat more elaborated with a temperature-dependent specific heat capacity, since the term  $cT_j$  in Eq. (12) needs to be replaced by the integral  $\int_0^{T_j} c(T) dT$ . Due to the simplicity of the numerical scheme, it is also rather simple to include energy sink and source terms accounting for, e.g., ice sublimation and condensation.

When the code is run in 3D mode, the results will only be valid for a terrain having the same physical dimensions as the domain under consideration. Since a volume element needs to be small compared to the thermal skin depth, and since there is a practical limitation on the number of volume elements that it is feasible to use, the considered domain will be rather small. For example, if thermophysics requires the usage of millimeter-sized cells, the considered surface will typically be a few centimeters across, the size scale of surface topography is limited to a few millimeters, and the depth of the domain needs to be a few decimeters. Thus, 3D simulations are suitable when studying small laboratory samples, detailed thermophysical properties of small patches of planetary surfaces resolved by landers or rovers, or statistical properties of emission from larger pieces of terrain that is planar on size scales above a few centimeters (i.e., when the small simulated topography can be considered *representative* of a larger region).

When the code is run in 1D mode, arbitrarily large terrains can be studied. This is because the illumination conditions are *scale free* (particularly, view factors only depend on the ratio  $s_k/r^2$  and remain constant when terrain sizes are scaled up or down), and vertical columns of volume elements do not communicate with each other. To model the top decimeter surface layer of a 100 m crater with millimeter resolution, is therefore equivalent to considering a cm-sized crater on top of a decimeter-deep column, resolved by mm-sized cells.

We finally note that several tests have been performed to verify the correctness of various aspects of our code. The basic thermophysical performance has been tested by comparing our code with a standard finite element method solver developed by one of us (Davidsson) for a plane-parallel medium with 1D heat conduction. An example is seen in Fig. 2. We have also made detailed tests for irregular topographies with 1D heat conduction by comparing with simulations performed using the finite difference code of Gutiérrez et al. (2001). In both cases, temperature solutions and view factor properties are the same to within small differences caused by the practical difficulty of running completely identical simulations. In the current paper, we derive analytical solutions for various problems including 3D heat conduction, and demonstrate that our code yields the expected solutions. With educated guesses of the initial temperature  $T_0$  based on balancing the average insolation with thermal emission, we typically run the code for 10 revolutions to reach steady state. At steady state, no net loss or release of energy due to heating and cooling of sub-surface regions during a revolution are expected. Thus, if the code conserves energy, the thermal losses should match the absorbed solar energy when integrated over a rotational period (in both cases, using view factors to calculate actual absorption and emission based on the acquired

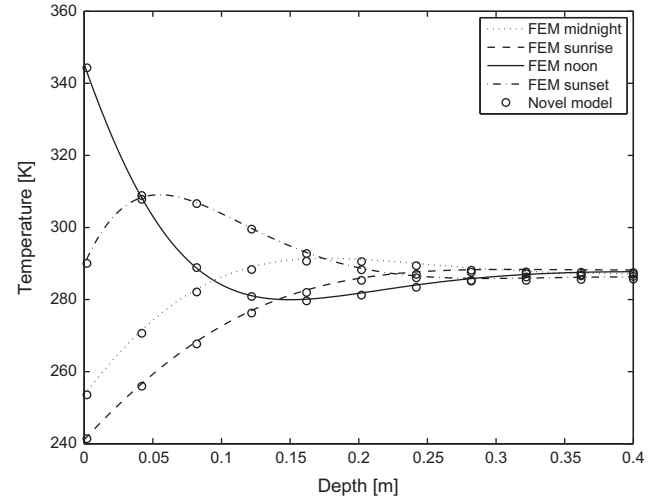


**Fig. 2.** Temperature versus depth at midnight, sunrise, noon and sunset according to a Finite Element Method (FEM) solver (curves), and the 3D code run in 1D mode (circles), considering  $P = 40$  h,  $\Gamma = 1184$  MKS,  $r_h = 1$  AU,  $i_{co} = 90^\circ$ , and the spin axis perpendicular to the orbital plane.

temperatures). The simulations presented in this work fulfill this expectation to within 0.2–1.3%.

## 2.6. Spectral energy distributions of resolved targets

The code was originally written in order to calculate emission from an unresolved patch of rough terrain seen at a specific illumination and viewing geometry on a well-resolved body. This is done by placing the observer at a given position in the equatorial system, and transforming this position vector into the surface system for a given co-latitude and rotational phase,  $\mathbf{p}_{obs,ss}$ . This fixes the incidence angle  $i$  (the angle between the solar position vector  $\hat{\mathbf{S}}_{\odot,ss}$  and the average surface normal  $\mathbf{Z}_{ss}$ ) at the time of observation, and defines the incidence plane (containing  $\hat{\mathbf{S}}_{\odot,ss}$  and  $\mathbf{Z}_{ss}$ ). It also fixes the emergence angle  $e$  (the angle between the position vector  $\mathbf{p}_{obs,ss}$  of the observer and the average surface normal  $\mathbf{Z}_{ss}$ ), and defines the emergence plane (containing  $\mathbf{p}_{obs,ss}$  and  $\mathbf{Z}_{ss}$ ). Finally, it fixes the azimuth angle  $\psi$ , which is the angle measured from the incidence plane, counter-clockwise about  $\mathbf{Z}_{ss}$  towards the emergence plane.

In order to calculate the infrared Spectral Energy Distribution (SED) corresponding to a certain set  $\{i, e, \psi\}$ , the surface temperatures  $T_{sj}$  are first used to evaluate the corresponding Planck functions,

$$B_j(\lambda) = \epsilon \frac{2h_p c_v^2}{\lambda^5} \left( \exp \left( \frac{h_p c_v}{k_B \lambda T_{sj}} \right) - 1 \right)^{-1} \quad (18)$$

in SI units, which is multiplied by  $10^{-6}$  to yield the unit ( $\text{W m}^{-2} \text{sr}^{-1} \mu\text{m}^{-1}$ ), i.e., we express the spectral radiance per micrometer wavelength instead of per meter. The wavelength, Planck constant, speed of light, and Boltzmann constant are denoted by  $\lambda$ ,  $h_p$ ,  $c_v$ , and  $k_B$ , respectively. The SED is then calculated as

$$\mathcal{I}(\lambda) = \frac{\sum_{j=1}^{N_{fac}} B_j(\lambda) s_j \cos e_j v_{j,obs}}{\sum_{j=1}^{N_{fac}} s_j \cos e_j v_{j,obs}}. \quad (19)$$

Here,  $v_{j,obs}$  is a visibility switch that is unity if the observer can see facet  $j$  and zero if the facet is turned away ( $e > 90^\circ$ ), or is hidden behind topography. The presence of  $v_{j,obs}$  makes the spectral radiance  $\mathcal{I}(\lambda)$  of rough surfaces highly dependent on  $e$  and  $\psi$ , which is not the case for a planar surface ( $B_j$  itself lacks  $e$ - and  $\psi$ -dependence).

We note that modeled positive relief terrain of finite size may exhibit undesirable edge effects. For example, when the incidence angle is large, the Sun may strongly illuminate the walls of convex features, that would have been in shadow if external terrain had been modeled as well. Walls of convex structures near the edge of the modeled terrain, that are not receiving direct sunlight, may be much cooler than would have been the case if they received a self heating flux from surrounding unmodeled terrain. We therefore have a routine that allows us to cut out the edges, and only calculate  $\mathcal{I}(\lambda)$  for an internal fraction of the terrain. The cut-out boundary of the domain is allowed to shadow and self-heat internal terrain, as well as hiding it from the view of an observer at large emergence angles, but does not contribute to the observed spectral radiance. Thus, quasi-cyclic boundary conditions can be simulated.

### 2.7. Spectral energy distributions of disk-integrated targets

We have also developed a routine to calculate the disk-integrated SEDs of spherical targets covered by small-scale surface roughness. The routine divides the macroscopic body into typically  $5^\circ \times 5^\circ$  or  $10^\circ \times 10^\circ$  longitudinal and latitudinal patches, each characterized by its own set of  $\{i, e, \psi\}$  depending on the orientation of the body and location of the observer. The disk-integrated spectral radiance is the sum of the spectral radiances of each patch (calculated as in Section 2.6), weighted by the fractional projected surface area of the patches. This allow us to calculate, e.g., the thermal infrared phase function of minor Solar System bodies with small-scale surface roughness and non-zero thermal inertia, fully accounting for day- and night-side emission effects. The code currently does not support global irregularity, but it could be extended to non-spherical bodies without too much efforts, should a need arise. We have verified that our disk-integrated  $10.6 \mu\text{m}$  phase curve of Asteroid (1) Ceres matches observations, when using the same roughness model, degree of roughness and thermal inertia as [Spencer \(1990\)](#). A figure that compares the observed magnitude of Ceres versus phase angle with our model calculations is shown by [Davidsson et al. \(2014\)](#).

The symbols used in the thermophysical model have been collected in [Table 1](#) for reference. Other symbols used in this paper are summarized in [Table 2](#).

## 3. Theory

We here discuss view factors (Section 3.1) and three different parameters that measure the level of surface roughness (Section 3.2). We then derive relations between these roughness parameters valid for a multiple scattering concave spherical segment (Section 3.3) and use this to define boundary condition corrections to be used in 1D models, in order to reproduce 3D heat conduction models for such a topography in the  $D \ll L$  limit (Section 3.4). Finally, a similar boundary condition is derived for arbitrary topographies in the single scattering limit (Section 3.5).

### 3.1. View factors

Consider two facets  $j$  and  $k$ . Facet  $j$  has surface area  $s_j$  and emits the isotropic spectral radiance  $I_j$ . Facet  $k$  is considered a collector of radiation from  $j$ , and has surface area  $s_k$ . They are located at a distance  $r$  from each other, with surface normals  $\hat{n}_j$  and  $\hat{n}_k$ . The angles between these normals and the line joining the facets are  $\theta_j < 90^\circ$  and  $\theta_k < 90^\circ$ , respectively. The line between  $j$  and  $k$  is free from obstructions. The total power  $P_j$  produced by facet  $j$  is,

$$P_j = \int_0^{2\pi} \int_0^{\frac{\pi}{2}} I_j s_j \cos \vartheta \sin \vartheta d\vartheta d\phi = \pi I_j s_j, \quad (20)$$

where  $\vartheta$  and  $\phi$  are the polar and azimuth angles, respectively, of a spherical coordinate system with  $\vartheta = 0^\circ$  corresponding to  $\hat{n}_j$ . A fraction of this emitted power  $dP_{jk}$  will be intercepted by the facet  $k$ . This fraction is calculated by multiplying  $I_j$  by the projected collecting surface area, and by the solid angle of the emitter as seen from  $k$ , i.e.,

$$dP_{jk} = I_j s_k \cos \theta_k \frac{s_j \cos \theta_j}{r^2}. \quad (21)$$

We now define the view factor  $\mathcal{F}_{jk}$  as

$$\mathcal{F}_{jk} = \frac{dP_{jk}}{P_j} = \frac{s_k \cos \theta_j \cos \theta_k}{\pi r^2}, \quad (22)$$

which is identical to Eq. (1), remembering that  $v_{jk} = 1$ .

From this definition, it follows that

$$\mathcal{F}_{jk} s_j = \mathcal{F}_{kj} s_k, \quad (23)$$

known as the *reciprocity relation*. From Eqs. (22) and (23) follow two rather different physical interpretations of  $\mathcal{F}_{jk}$  of equal practical importance.

#1. The view factor  $\mathcal{F}_{jk}$  is the *fraction of power* produced by facet  $j$  that is illuminating facet  $k$ . Here, the entire facet surface areas  $s_j$  and  $s_k$  participate in the energy transfer.

#2. The view factor  $\mathcal{F}_{jk}$  is the *fraction of flux* produced by facet  $k$  that is illuminating facet  $j$ . Here, unit surface areas of both facets participate in the energy transfer.

A useful application of statement #1 is that the total fraction of the power produced by a facet  $j$  that is transmitted towards *all* other parts of the surface is

$$P_{\text{surf},j} = P_j \sum_{k \neq j} \mathcal{F}_{jk}, \quad (24)$$

while the fraction reaching space accordingly is

$$P_{\text{out},j} = P_j \left( 1 - \sum_{k \neq j} \mathcal{F}_{jk} \right). \quad (25)$$

Statement #2 follows when a flux  $F_k$  ( $\text{J m}^{-2} \text{s}^{-1}$ ) is produced by a facet  $k$ , so that its emitted power is  $P_k = F_k s_k$  ( $\text{J s}^{-1}$ ), of which the fraction  $\mathcal{F}_{kj} F_k s_k$  ( $\text{J s}^{-1}$ ) is passed to facet  $j$  in its entire. Thus, the *flux* illuminating facet  $j$  is  $\mathcal{F}_{kj} F_k s_k / s_j$  ( $\text{J m}^{-2} \text{s}^{-1}$ ), or according to Eq. (23), it is equal to  $F_k \mathcal{F}_{jk}$  ( $\text{J m}^{-2} \text{s}^{-1}$ ). A useful application of statement #2 is that the total flux illuminating a facet  $j$  from the surrounding surface, i.e., the *self heating flux*, is

$$F_{\text{sh},j} = \sum_{k \neq j} F_k \mathcal{F}_{jk}. \quad (26)$$

### 3.2. Measures of surface roughness

It is often necessary to describe the *degree* of roughness of a surface. Commonly used parameters include the [Hapke \(1984\)](#) mean slope angle  $\bar{\theta}$ , the RMS mean slope angle  $s_{\text{rms}}$  (e.g., [Spencer, 1990](#)), and the RMS of slopes  $q$  ([Lagerros, 1998](#)). However, such geometric averages of facet tilt angles are not necessarily suitable for describing the thermophysical properties of a terrain. The *small scale self heating parameter* (e.g., [Lagerros, 1997](#)) is an interesting alternative to  $\bar{\theta}$ ,  $s_{\text{rms}}$  and  $q$  since it measures the degree of self heating *caused* by roughness. It is defined as a power ratio,

$$\chi_p = \frac{P_{\text{sh}}}{P_{\text{prod}}} = \frac{P_{\text{prod}} - P_{\text{out}}}{P_{\text{prod}}} = 1 - \frac{P_{\text{out}}}{P_{\text{prod}}}, \quad (27)$$

**Table 1**

Symbols used in the thermophysical model.

Symbol	Description	Symbol	Description
$A$	Bond albedo	$k_B$	Boltzmann constant
$B$	Planck function	$l_{co}$	Co-latitude
$D$	Roughness size scale	$\hat{n}$	Facet normal unit vector
$\mathcal{E}$	Internal energy	$\mathbf{p}_{obs}$	Location of observer
$\mathcal{F}_{jk}$	View factor	$r$	Distance between two facets or volume elements
$\mathcal{I}$	Spectral radiance	$r_h$	Heliocentric distance
$L$	Thermal skin depth	$s$	Facet area
$M$	Rotational transformation matrix	$t$	Time
$N_{fac}$	Number of facets	$u$	Direct thermal flux
$N_{ms}$	Number of iterations	$v_{jk}$	Visibility between facets $j, k$
$\mathcal{P}$	Rotational period	$v_{j,obs}$	Visibility between facet $j$ and observer
$S_{\odot}$	Solar constant	$v_{j\odot}$	Visibility between facet $j$ and Sun
$\hat{S}_{\odot}$	Solar unit position vector	$w$	Diffuse thermal flux
$T$	Temperature	$x, y, z$	Cartesian coordinates
$U$	Direct solar flux	$\hat{x}, \hat{y}, \hat{z}$	Cartesian unit principal axes
$V$	Cell volume	$\Delta t$	Time step
$W$	Diffuse solar flux	$\Delta x, \Delta y, \Delta z$	Volume cell dimensions
$\gamma^{(i)}$	Diffuse solar flux during iteration $i$	$\Delta z_j$	Distance from surface to upper cell center
$\mathcal{W}_{lim}$	Diffuse solar flux threshold	$\alpha$	Right ascension
$\mathbf{X}, \mathbf{Y}, \mathbf{Z}$	Cartesian principal axes	$\delta$	Declination
$a_{jl}$	Contact area between cells $j, l$	$\varepsilon$	Emissivity
$c$	Specific heat capacity	$\theta_j$	Tilt angle of facet $j$ w.r.t. global normal
$c_v$	Speed of light in vacuum	$\kappa$	Heat conductivity
$d$	Rotational phase angle	$\lambda$	Wavelength
$e$	Emergence angle	$\mu$	Cosine of incidence angle
$h_p$	Planck constant	$\rho$	Mass density
$i$	Incidence angle	$\sigma$	Stefan–Boltzmann constant
$i$	Iteration index	$\psi$	Azimuth angle
$j, k$	Facet indexes	$\omega$	Angular velocity
$j, l$	Volume cell index	$\varpi^{(i)}$	Diffuse thermal flux during iteration $i$

**Table 2**

Symbols used in the theoretical investigation.

Symbol	Description	Symbol	Description
$A_{eff}^{ms}$	Effective Bond albedo (mult. scatt.)	$S_1$	Area of flat terrain
$A_{eff}^{ss}$	Effective Bond albedo (sing. scatt.)	$T_{bb}$	Blackbody temperature
$A_{IR}$	Infrared albedo	$T_{flat}$	Sub-solar point temperature of flat terrain
$A_{obs}$	Observed Bond albedo	$T_{ss}$	Convex spherical segment temperature
$A_v$	Visual albedo	$dP_{jk}$	Power from facet $j$ intercepted by facet $k$
$F_{heat}$	Net heating flux	$dx, dy$	Dimensions of surface area element
$F_j$	Flux emitted by facet $j$	$f_{abs}$	Absorb./illum. self heating power ratio
$F_{\odot}$	Solar flux at target	$h$	Depth (height) of spherical segment crater (hill)
$G_j$	Irradiation of facet $j$	$p$	Facet index
$I_j$	Spectral radiance from facet $j$	$s_{rms}$	RMS mean slope angle
$J_j$	Thermally emitted flux from facet $j$	$x_{min}, x_{max}$	Integration limits
		$y_{min}, y_{max}$	
$\mathcal{K}$	Heat conduction flux	$\Gamma$	Thermal inertia
$P_{bb}$	Power emitted by blackbody	$\Delta T$	Temperature difference
$P_j$	Power produced by facet $j$	$\beta, \gamma$	Auxiliary functions
$P_{abs}$	Solar power absorbed by terrain	$\varepsilon_{eff}^{ms}$	Effective emissivity (mult. scatt.)
$P_{cond}$	Vertically conducted power for terrain	$\varepsilon_{eff}^{ss}$	Effective emissivity (sing. scatt.)
$P_{heat}$	Net heating power	$\varepsilon_{0-0}$	Hemispherical emissivity of spherical segment
$P_{illum}$	Illuminating self heating power	$\varepsilon_{ID}$	Infrared emissivity
$P_{out}$	Escaping thermal power	$\bar{\theta}$	Hapke mean slope angle
$P_{prod}$	Produced thermal power	$\vartheta, \phi$	Spherical system polar, azimuth angles
$P_{sh}$	Absorbed self heating power	$\zeta$	Small scale roughness parameter
$R, R_{rim}$	Curvature/rim radius of spherical segment	$\tilde{\zeta}_{crat}$	$\tilde{\zeta}$ of spherical segment
$S$	Depth to curvature diameter ratio	$Q$	RMS of slopes
$S_c$	Surface area of spherical segment	$\sigma_T$	Standard deviation of surface temperature
$S_{flat}$	Projected area of rough terrain	$\chi$	Small scale self heating parameter (view factors)
$S_{rough}$	Surface area of rough terrain	$\chi_P$	Small scale self heating parameter (power)
$S_0$	Area enclosed by spherical segment rim	$\chi_{P, crat}$	$\chi_P$ of spherical segment

where  $P_{prod}$  is the thermal emission power produced by a terrain, of which an amount  $P_{sh}$  is re-absorbed by the surface since the hemispherical field of view of any given surface point partially is obstructed by surrounding terrain. Thus,  $P_{sh}$  is the self heating

power in the thermal infrared. The remaining amount  $P_{out} = P_{prod} - P_{sh}$  of the produced power is escaping to space. The small scale self heating parameter therefore measures the capability of the terrain to retain the radiation it produces, that generally



increases with the level of roughness. Note that  $P_{\text{prod}}$  can be substantially higher than the absorbed solar power  $P_{\text{abs}}$  as long as  $P_{\text{sh}}$  is such that  $P_{\text{abs}} = P_{\text{out}}$  to up-hold energy conservation.

It is sometimes possible to express  $\chi_p$  purely in terms of *geometric* properties of the surface. From Eq. (26) it is clear that the total power from facets  $k$  illuminating a facet  $j$  is  $s_j \sum_{k \neq j} \epsilon \sigma T_k^4 \mathcal{F}_{jk}$ . The total self-illumination is obtained by adding up the power received by all facets  $j$ ,

$$P_{\text{illum}} = \sum_j \left( \sum_{k \neq j} \epsilon \sigma T_k^4 \mathcal{F}_{jk} \right) s_j. \quad (28)$$

If the surface facets scatter a fraction  $A$  of the incident power, some of this energy may find its way to space through subsequent scattering events. Therefore,  $P_{\text{sh}}$  is given by

$$P_{\text{sh}} = f_{\text{abs}} P_{\text{illum}} = f_{\text{abs}} \sum_j \left( \sum_{k \neq j} \epsilon \sigma T_k^4 \mathcal{F}_{jk} \right) s_j \quad (29)$$

where  $f_{\text{abs}} = 1 - A$  if all scattered radiation escapes to space, and  $f_{\text{abs}} = 1$  only is certain when  $A = 0$  (we are here not concerned with completely closed cavities, only those seeing free space at least to some extent). Since the total production is given by,

$$P_{\text{prod}} = \sum_j \epsilon \sigma T_j^4 s_j, \quad (30)$$

Eqs. (27)–(30) yields,

$$\chi_p = \frac{f_{\text{abs}} \sum_j \left( \sum_{k \neq j} \epsilon \sigma T_k^4 \mathcal{F}_{jk} \right) s_j}{\sum_j \epsilon \sigma T_j^4 s_j}. \quad (31)$$

Lagerros (1997, 1998) argued that the small scale self heating parameter could be expressed as a *purely* geometric quantity,

$$\chi = \frac{\sum_j \left( \sum_{k \neq j} \mathcal{F}_{jk} \right) s_j}{\sum_j s_j} \quad (32)$$

as long as the surface is isothermal, i.e.,  $T_j = T_k = T$ . However, from Eq. (31) it is also clear that an additional condition is necessary to guarantee  $\chi = \chi_p$ . No scattering can be allowed, in order to make sure that  $f_{\text{abs}} = 1$ , i.e., in practice we require  $A = 0$ . For these reasons we here reserve the symbol  $\chi_p$  for the small scale self heating parameter based on the power ratio and distinguish it from  $\chi$ , which is the small scale self heating parameter based on view factors. This distinction is only erased for isothermal non-scattering surfaces.

Finally, a conceptually simple measure of surface roughness is defined. Based on the total surface area of a rough terrain  $S_{\text{rough}} = \sum_j s_j$  and its flat projected footprint area  $S_{\text{flat}}$ , we define the parameter  $\xi$  as

$$\xi = 1 - \frac{S_{\text{flat}}}{S_{\text{rough}}}. \quad (33)$$

According to Lagerros (1997, 1998) the small scale self heating parameter  $\chi$  is simply equal to  $\xi$ . Thus,  $\xi$  could potentially be a parameter with a profound physical meaning, in spite of its simplicity. Therefore, Davidsson et al. (2009) used  $\chi$  and  $\xi$  interchangeably, since the latter is far easier to calculate in practice, than the former. However, we will demonstrate that  $\chi = \xi$  only for certain terrain types. Therefore, we here make a distinction between the view factor-version of the small scale *self heating* parameter  $\chi$  and the small scale *roughness* parameter  $\xi$  (thereby keeping the name accidentally used by Davidsson et al., 2013).

### 3.3. The multiple-scattering concave spherical segment

We now derive a relation between  $\chi_p$  and  $\xi$  for a geometrically simple shape, the concave spherical segment, i.e., a crater with a depth  $h$  smaller than or equal to its curvature radius  $R$ . To distinguish these parameters from those of other terrains, they are here denoted  $\chi_{\text{p,crat}}$  and  $\xi_{\text{crat}}$ . We assume that the crater interior emits and scatters radiation diffusely, having an arbitrary Bond albedo  $A$  and an emissivity  $\epsilon = 1 - A$ . Let  $P_{\text{bb}}$  be the power emitted by a blackbody with temperature  $T_{\text{bb}}$  and a surface area  $S_0$  equal to the flat area enclosed by the crater rim,

$$P_{\text{bb}} = \sigma T_{\text{bb}}^4 S_0. \quad (34)$$

Now assume that the isothermal crater interior also has temperature  $T_{\text{bb}}$ , and that any emitted photon may scatter repeatedly, until absorbed or managing to exit through the crater opening. If the emerging power is  $P_{\text{out}}$ , the hemispherical emissivity is  $\epsilon_{0-0} = P_{\text{out}}/P_{\text{bb}}$ . This hemispherical emissivity may differ from unity, i.e., the crater may not emit like a blackbody.

Chandos and Chandos (1974) calculated  $\epsilon_{0-0}$  for a concave spherical segment with an isothermal, diffuse, gray interior. According to their result and Eq. (34)

$$P_{\text{out}} = \epsilon_{0-0} P_{\text{bb}} = \frac{\epsilon \sigma T_{\text{bb}}^4 S_0}{1 - (1 - \epsilon) \left\{ 1 - \frac{S_0}{S_c} \right\}} = \frac{\epsilon \sigma T_{\text{bb}}^4 S_0}{1 - (1 - \epsilon) \xi_{\text{crat}}}. \quad (35)$$

Here,  $S_c$  is the surface area of the crater interior, and since the rim area  $S_0$  equals the flat footprint of the crater, the expression within the curly brackets equals  $\xi_{\text{crat}}$ .

The total power produced by the crater interior is

$$P_{\text{prod}} = \epsilon \sigma T_{\text{bb}}^4 S_c, \quad (36)$$

of which a fraction  $\chi_{\text{p,crat}}$  is re-absorbed, while a fraction  $1 - \chi_{\text{p,crat}}$  exits into space. Therefore,  $P_{\text{out}}$  can also be written as,

$$P_{\text{out}} = (1 - \chi_{\text{p,crat}}) \epsilon \sigma T_{\text{bb}}^4 S_c. \quad (37)$$

Setting Eq. (35) equal to Eq. (37) and solving for  $\chi_p$  yields,

$$\chi_{\text{p,crat}} = \left( \frac{1 - A}{1 - \xi_{\text{crat}} A} \right) \xi_{\text{crat}}. \quad (38)$$

Eq. (38) shows that  $\chi_{\text{p,crat}} \rightarrow \xi_{\text{crat}}$  as  $A \rightarrow 0$ . But when no scattering takes place, the conditions for equality between Eqs. (32) and (27) are fulfilled, so that  $\chi_{\text{crat}} = \chi_{\text{p,crat}}$ . Thus,  $\chi_{\text{crat}} = \xi_{\text{crat}}$  for the concave spherical segment, verifying the statement of Lagerros (1997, 1998), for this particular topography. Eq. (38) also shows that  $\chi_{\text{p,crat}} \neq \chi_{\text{crat}}$  when  $A > 0$ , i.e., the small scale self heating parameter based on view factors does not *necessarily* measure the power retained by the surface with respect to production. Next, we calculate the flux balance to be used as boundary condition in a 1D model in order to reproduce 3D simulations of concave spherical segments with  $D \ll L$ .

### 3.4. Concave spherical segments with flat surroundings

We now consider a concave spherical segment with surface area  $S_c$  and rim area  $S_0$ , being surrounded by a finite flat terrain with area  $S_1$ . The material itself is characterized by Bond albedo  $A$ , emissivity  $\epsilon$ , heat conductivity  $\kappa$ , and is fully multiple scattering. The terrain is located on a rotating body that is heated by solar illumination. The rotational period is such that the thermal skin depth is far larger than the size of the crater, making the terrain isothermal at any given moment. The task is to calculate how the boundary condition in a standard 1D flat-surface thermophysical model should be formulated in order to *mimic* the temperature time-dependence of a 3D heat conduction model of the cratered terrain.

We show that the material albedo and emissivity  $\{A, \varepsilon\}$  need to be replaced by *effective counterparts* denoted  $\{A_{\text{eff}}^{\text{ms}}, \varepsilon_{\text{eff}}^{\text{ms}}\}$  in a multiple-scattering scenario, and  $\{A_{\text{eff}}^{\text{ss}}, \varepsilon_{\text{eff}}^{\text{ss}}\}$  in the single-scattering limit.

We need to consider the power balance of the surface and start by calculating the absorbed power  $P_{\text{abs}}$ . The power entering the crater is  $S_{\odot}\mu S_0/r_h^2$  of which a fraction  $(1-A)$  is absorbed immediately while a fraction  $A$  is scattered. Here,  $S_{\odot}$  is the solar constant,  $\mu = \cos i$  where  $i$  is the incidence angle of the Sun (measured from the surface normal of the flat terrain), and  $r_h$  is the heliocentric distance. The amount of scattered radiation that eventually becomes absorbed is  $S_{\odot}\mu A S_0 \chi_{\text{P,crat}}/r_h^2$ . Finally, the power absorbed by the surrounding flat terrain must be added, which yields,

$$P_{\text{abs}} = \frac{S_{\odot}\mu}{r_h^2} (S_1(1-A) + S_0[1 - (1 - \chi_{\text{P,crat}})A]). \quad (39)$$

It is not self-evident that Eq. (38) can be used to evaluate  $\chi_{\text{P,crat}}$  in Eq. (39). The former equation was derived under the assumption that all parts of the crater interior constituted equal flux sources (thermally emitted photons from an isothermal crater). Considering the first generation of scattered photons in the current case, their fluxes depend strongly on position within the crater due to varying illumination conditions. If the probability of photon escape varies with place of origin, Eq. (38) cannot be applied. Fortunately, all facet pairs  $\{j, k\}$  in a spherical geometry have  $\theta_k = \theta_j$  and  $r = 2R \cos \theta_j$ , thus  $\mathcal{F}_{jk} = S_k/4\pi R^2$  according to Eq. (22). Summing  $1 - \mathcal{F}_{jk}$  over all  $k$  yields identical escape probabilities  $S_c/4\pi R^2$  for all  $j$ . Thus, Eq. (38) can be applied also in the current context.

The total emitted and escaping power is the radiation originating from the flat terrain, plus the contribution from the crater according to Eq. (37). Due to the efficient heat conduction, all parts of the surface will have the same temperature  $T$ ,

$$P_{\text{out}} = \varepsilon \sigma T^4 (S_1 + (1 - \chi_{\text{P,crat}})S_c). \quad (40)$$

The difference  $P_{\text{abs}} - P_{\text{out}}$  equals the power  $P_{\text{cond}}$  conducted from the surface towards the interior, or vice versa, depending on the sign. For a 1D model, only conduction along the vertical direction is of importance. Thus, if a facet  $j$  has an inward normal  $\hat{n}_j$  that tilts an angle  $\theta_j$  with respect to the inward normal  $\hat{n}_f$  of the flat surface, its contribution to the transfer of power along  $\hat{n}_f$  is

$$P_{\text{cond}j} = -S_j \cos \theta_j \kappa \frac{dT}{dz}, \quad (41)$$

where  $z$  is the depth coordinate along  $\hat{n}_f$ . Integrating Eq. (41) over the terrain yields

$$P_{\text{cond}} = -(S_1 + S_0) \kappa \frac{dT}{dz}. \quad (42)$$

In order to transform the power balance  $P_{\text{abs}} = P_{\text{out}} + P_{\text{cond}}$  into a flux balance, we divide by the total surface area  $S_1 + S_c$ , thereby obtaining,

$$\begin{aligned} & \frac{S_{\odot}\mu}{r_h^2} \frac{(S_1(1-A) + S_0[1 - (1 - \chi_{\text{P,crat}})A])}{S_1 + S_c} \\ &= \varepsilon \sigma T^4 \frac{S_1 + (1 - \chi_{\text{P,crat}})S_c}{S_1 + S_c} - \frac{S_1 + S_0}{S_1 + S_c} \kappa \frac{dT}{dz} \end{aligned} \quad (43)$$

Eq. (43) can be re-written as

$$\frac{S_{\odot}(1 - A_{\text{eff}}^{\text{ms}})\mu}{r_h^2} = \varepsilon_{\text{eff}}^{\text{ms}} \sigma T^4 - \kappa \frac{dT}{dz} \quad (44)$$

by recognizing that the factor  $(S_1 + S_0)/(S_1 + S_c)$  in the second right hand term equals  $S_{\text{flat}}/S_{\text{rough}} = 1 - \xi$  for the entire terrain (flat regions and the crater) according to Eq. (33) and by defining the effective albedo  $A_{\text{eff}}^{\text{ms}}$  and emissivity  $\varepsilon_{\text{eff}}^{\text{ms}}$  in this multiple-scattering version as,

$$\begin{cases} A_{\text{eff}}^{\text{ms}} = \frac{S_c(1-\xi) + S_1(A-\xi) - S_0[1 - (1 - \chi_{\text{P,crat}})A]}{(S_1 + S_c)(1-\xi)} \\ \varepsilon_{\text{eff}}^{\text{ms}} = \varepsilon \frac{S_1 + (1 - \chi_{\text{P,crat}})S_c}{(S_1 + S_c)(1-\xi)} \end{cases} \quad (45)$$

Eq. (44) is the boundary condition for 1D models we set out to find, that mimics 3D heat conduction models of a cratered surface, as long as  $D \ll L$  and multiple-scattering is taken into account in the latter. Note that  $A \rightarrow 0$  and  $\varepsilon \rightarrow 1$  means that  $A_{\text{eff}}^{\text{ms}} \rightarrow 0$  and  $\varepsilon_{\text{eff}}^{\text{ms}} \rightarrow 1$  according to Eq. (45). Thus, terrain containing spherical segment craters are thermally indistinguishable from flat terrain if  $A = 0$  and  $\varepsilon = 1$ . This is ultimately because  $\varepsilon_{0-0} = 1$  and  $\chi_{\text{P,crat}} = \xi_{\text{crat}}$  in this case. However, systematic temperature differences between flat and cratered terrain are expected when  $A \neq 0$  and  $\varepsilon \neq 1$  since  $A_{\text{eff}}^{\text{ms}} \neq A$  and  $\varepsilon_{\text{eff}}^{\text{ms}} \neq \varepsilon$ , caused by  $\chi_{\text{P,crat}} \neq \xi_{\text{crat}}$ .

The previous discussion is valid for gray bodies that have the same albedo at all wavelengths. However, with a small adjustment, Eq. (45) can also be applied for materials that have different reflectivity at visual and thermal infrared wavelengths. The visual albedo  $A_V$  (monochromatic hemispherical reflectance integrated over the visual part of the spectrum) is used to evaluate  $\chi_{\text{P,crat}}$  according to Eq. (38) and both are inserted into Eq. (45) to evaluate  $A_{\text{eff}}^{\text{ms}}$ . Then the infrared albedo  $A_{\text{IR}}$  (monochromatic hemispherical reflectance integrated over the infrared part of the spectrum) is used to evaluate *another*  $\chi_{\text{P,crat}}$ -value with Eq. (38), that goes into Eq. (45) along with the emissivity  $\varepsilon_{\text{IR}} = 1 - A_{\text{IR}}$  to evaluate  $\varepsilon_{\text{eff}}^{\text{ms}}$ .

The single scattering limit means that the fraction of re-captured photons is increased from  $\chi_{\text{P,crat}}$  to  $\chi_{\text{crat}}$ . Thus, replacing  $\chi_{\text{P,crat}}$  by  $\chi_{\text{crat}}$  in Eq. (45) yields the single scattering versions of the effective albedo and emissivity,

$$\begin{cases} A_{\text{eff}}^{\text{ss}} = \frac{S_c(1-\xi) + S_1(A-\xi) - S_0[1 - (1 - \chi_{\text{crat}})A]}{(S_1 + S_c)(1-\xi)} \\ \varepsilon_{\text{eff}}^{\text{ss}} = \varepsilon \frac{S_1 + (1 - \chi_{\text{crat}})S_c}{(S_1 + S_c)(1-\xi)} \approx \varepsilon \end{cases} \quad (46)$$

The relation  $\varepsilon_{\text{eff}}^{\text{ss}} \approx \varepsilon$  follows from the fact that  $\chi_{\text{crat}} = \xi_{\text{crat}}$  for spherical segments. However, since the limited resolution on numerical realizations of craters may ruin the exact equivalency between  $\chi_{\text{crat}}$  and  $\xi_{\text{crat}}$ , we caution that  $\varepsilon_{\text{eff}}^{\text{ss}}$  may not be exactly equal to  $\varepsilon$  in practice. This is seen in Table 3, which contains examples of effective albedo and emissivity for various material  $\{A, \varepsilon\}$ .

### 3.5. General topographies near the single scattering limit

The discussion in Sections 3.3 and 3.4 is restricted to a concave spherical segment, with or without surrounding flat terrain. We here take steps towards the analytical consideration of an arbitrary topography, improving upon an earlier estimate (Davidsson et al., 2009, Appendix B). Due to the complexity of the problem, several approximations are made that are valid when  $A \approx 0$ .

**Table 3**

A spherical segment with curvature radius  $R = 0.02040$  m and depth  $h = 0.01080$  m has a rim radius  $R_{\text{rim}} = 0.01800$  m and depth-to-diameter ratio  $h/2R = 0.26471$ . If located on a  $0.04000 \times 0.04000$  m<sup>2</sup> flat terrain, the terrain has  $\xi = \chi = 0.1863$ , while  $\xi_{\text{crat}} = 0.26471$  (it equals  $h/2R$ ). An 800-facet numerical realization of this terrain, seen in the upper left panel of Fig. 1 has  $S_1 = 4.8400 \times 10^{-4}$  m<sup>2</sup>,  $S_c = 1.4641 \times 10^{-3}$  m<sup>2</sup>,  $S_0 = 1.1160 \times 10^{-3}$  m<sup>2</sup>,  $\xi_{\text{crat}} = 0.24162$ ,  $\xi = 0.17869$ , and  $\chi = 0.18159$ . Given the albedo  $A$  and emissivity  $\varepsilon$  of a surface material, these parameters are used to evaluate the effective albedo  $A_{\text{eff}}^{\text{ms}}$  and effective emissivity  $\varepsilon_{\text{eff}}^{\text{ms}}$  in the multiple scattering case according to Eq. (45), remembering that  $\chi_{\text{P,crat}}$  is obtained from Eq. (38). The effective albedo and emissivity in the single scattering approximation ( $A_{\text{eff}}^{\text{ss}}$  and  $\varepsilon_{\text{eff}}^{\text{ss}}$ ) are calculated from Eq. (46).

A	$\varepsilon$	$\chi_{\text{P,crat}}$	$A_{\text{eff}}^{\text{ms}}$	$\varepsilon_{\text{eff}}^{\text{ms}}$	$A_{\text{eff}}^{\text{ss}}$	$\varepsilon_{\text{eff}}^{\text{ss}}$
0.0	1.0	0.23775	0.00000	1.00000	0.00000	1.00000
0.2	0.8	0.19970	0.17214	0.82786	0.16629	0.79717
0.4	0.6	0.15764	0.35602	0.64399	0.33259	0.59788
0.6	0.4	0.11092	0.55358	0.44642	0.49888	0.39859
0.8	0.2	0.05872	0.76724	0.23277	0.66518	0.19929

The total flux illuminating a facet  $j$  is given by

$$G_j = \frac{S_\odot \mu_j v_{j\odot}}{r_h^2} + \sum_{k \neq j} \mathcal{F}_{jk} v_{jk} J_k, \quad (47)$$

and is called the *irradiation* (Lagerros, 1997). It consists of direct solar illumination, and radiation arriving from other facets  $k$  which produces a combined scattered and emitted flux  $J_k$ .

The total flux emerging from facet  $j$  is given by

$$J_j = AG_j + \varepsilon \sigma T_j^4 \quad (48)$$

and is called the *radiosity* (Lagerros, 1997). It consists of the fraction of irradiation that has scattered *once* and the thermal emission corresponding to the local temperature  $T_j$ . The difference between these fluxes is the conductive flux along the local surface normal

$$-\kappa \frac{dT}{dz_j} = G_j - J_j = (1 - A) \left( \frac{S_\odot \mu_j v_{j\odot}}{r_h^2} + \sum_{k \neq j} \mathcal{F}_{jk} v_{jk} J_k \right) - \varepsilon \sigma T_j^4. \quad (49)$$

Rearranging and substituting  $J_k$  according to Eq. (48) yields

$$\frac{S_\odot v_{j\odot} (1 - A) \mu_j}{r_h^2} = \varepsilon \sigma T_j^4 - (1 - A) \sum_{k \neq j} \mathcal{F}_{jk} v_{jk} (AG_k + \varepsilon \sigma T_k^4) - \kappa \frac{dT}{dz_j}. \quad (50)$$

The second term on the right hand side of Eq. (50) states that a fraction  $1 - A$  of scattered or emitted radiation arriving from other facets should be absorbed, implying that a fraction  $A$  is passed on. However, in the single scattering limit, secondary scattering is quenched and thermally emitted radiation never scatters. Thus the factor  $1 - A$  in the term in question must be replaced by unity. Also considering the term  $AG_k$  in Eq. (50),

$$AG_k = \frac{S_\odot v_{k\odot} A \mu_k}{r_h^2} + A \sum_{p \neq k} \mathcal{F}_{kp} v_{kp} J_p. \quad (51)$$

The first term represents direct solar radiation that has been scattered *once*, which must be included. However, the second term represent scattered or thermally emitted radiation arriving from elsewhere (all other facets  $p$ ), that is *passed on* by  $k$ . This contribution must be excluded in the single scattering formalism. We now force the terrain to be isothermal, by setting  $T_j = T_k = T$ . The resulting equation is multiplied by the surface area  $s_j$  of facet  $j$  to obtain the local power, and summed over  $j$  to obtain the *total power balance of the terrain*. In order to obtain the *average flux balance*, which can be reproduced by a 1D thermophysical model, we then divide by the total surface area. After re-arrangement we obtain,

$$\frac{S_\odot}{r_h^2} \left( (1 - A) \frac{\sum_j \mu_j v_{j\odot} s_j}{\sum_j s_j} + A \frac{\sum_j \left( \sum_{k \neq j} \mathcal{F}_{jk} \mu_k v_{k\odot} v_{jk} \right) s_j}{\sum_j s_j} \right) = \varepsilon \sigma T^4 \left( 1 - \frac{\sum_j \left( \sum_{k \neq j} \mathcal{F}_{jk} v_{jk} \right) s_j}{\sum_j s_j} \right) - \kappa \frac{1}{\sum_j s_j} \sum_j \frac{dT}{dz_j} s_j \quad (52)$$

The sums in Eq. (52) are now evaluated. The first term in the big brackets on the left hand side of Eq. (52) describes the average direct solar radiation flux absorbed by the surface. The sum in the nominator is the projected surface area of the terrain as seen from the Sun, i.e., the cross section that collects radiation. The denominator is trivially equal to  $S_{\text{rough}}$ , hence,

$$\frac{\sum_j \mu_j v_{j\odot} s_j}{\sum_j s_j} \approx \frac{\mu S_{\text{flat}}}{S_{\text{rough}}} = (1 - \xi) \mu. \quad (53)$$

The expression is approximate since  $\mu \rightarrow 0$  as the solar incidence angle  $i \rightarrow 90^\circ$ , while an irregular surface may still be partially illuminated if hills or mountains stick up above ground level.

Fig. 3 compares the analytical approximation (dashed-dotted) and the numerically evaluated sum in Eq. (53) for the negative relief random Gaussian terrain (asterisks) seen in the lower left panel of Fig. 1. The difference is small since there is no topography above ground level. However, if this surface is mirrored to produce a positive relief random Gaussian terrain (circles), differences increase somewhat at large incidence angles. Eq. (53) basically states that the absorbed flux is proportional to the cross section of the terrain as seen by the Sun ( $\mu S_{\text{flat}}$ ), but that this radiation is *smeared out* over a much larger area  $S_{\text{rough}}$ , so that the *average* flux available to a given surface point potentially may be small compared to that of a flat surface (solid curve). This could particularly be the case for fractal surfaces, that may have a high surface area for small footprints.

The second term in the big brackets on the left hand side of Eq. (52) describes the average flux of diffuse solar radiation absorbed by the surface. The terrain presents a cross section  $S_{\text{flat}} \mu$  to the Sun, and the total scattered amount is  $A S_{\text{flat}} \mu$ , of which a fraction  $\chi_p$  is retained. Thus,

$$\frac{A \sum_j \left( \sum_{k \neq j} \mathcal{F}_{jk} \mu_k v_{k\odot} v_{jk} \right) s_j}{\sum_j s_j} = \frac{A \mu S_{\text{flat}} \chi_p}{S_{\text{rough}}} = A \mu \chi_p (1 - \xi). \quad (54)$$

The first term on the right hand side of Eq. (52) describes the energy loss from the surface by thermal emission, adjusted for self heating. According to Eq. (32),

$$\varepsilon \sigma T^4 \left( 1 - \frac{\sum_j \left( \sum_{k \neq j} \mathcal{F}_{jk} v_{jk} \right) s_j}{\sum_j s_j} \right) = \varepsilon \sigma T^4 (1 - \chi). \quad (55)$$

The last term in Eq. (52) can be re-written in the following manner,

$$\begin{aligned} -\kappa \frac{1}{\sum_j s_j} \sum_j \frac{dT}{dz_j} s_j &= -\kappa \frac{1}{S_{\text{rough}}} \sum_j \frac{dT}{dz} \frac{s_j}{\cos \theta_j} \\ &= -\kappa \frac{1}{S_{\text{rough}}} \frac{dT}{dz} \sum_j \cos \theta_j s_j = -\frac{S_{\text{flat}}}{S_{\text{rough}}} \kappa \frac{dT}{dz} \\ &= -(1 - \xi) \kappa \frac{dT}{dz}. \end{aligned} \quad (56)$$

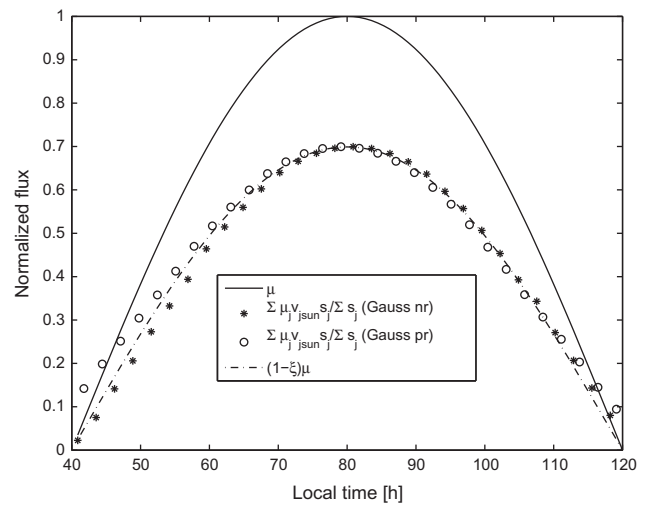


**Fig. 3.** The daytime solar flux on a flat surface versus time assuming a  $P = 160$  h period and a peak flux of unity (solid). This is compared to the flux on a negative relief (nr) random Gaussian terrain (the lower left panel in Fig. 1), averaged over the entire available surface area (asterisks), calculated according to the left hand side of Eq. (53). This surface is a mirrored version of the positive relief (pr) random Gaussian terrain (the lower left panel in Fig. 10), illuminated by an average flux shown by circles. The approximation on the right hand side of Eq. (53) is shown as a dashed-dotted curve.

If Eqs. (53)–(56) are inserted into Eq. (52) we obtain

$$\frac{S_{\odot}\mu}{r_h^2}((1-A)(1-\xi) + A\chi_p(1-\xi)) = (1-\chi)\varepsilon\sigma T^4 - (1-\xi)\kappa\frac{dT}{dz}. \quad (57)$$

Recognizing that  $(1-A)(1-\xi) \gg A\chi_p(1-\xi)$  when  $A \approx 0$ , we ignore the contribution of the second term in the big brackets on the left hand side, and conclude that,

$$\frac{S_{\odot}(1-A)\mu}{r_h^2} = \frac{(1-\chi)}{(1-\xi)}\varepsilon\sigma T^4 - \kappa\frac{dT}{dz}. \quad (58)$$

Eq. (58) illustrates an extremely important principle. *If the view factor version of the small scale self heating parameter  $\chi$  equals the small scale roughness parameter  $\xi$ , then a quasi-isothermal rough terrain with  $D/L \ll 1$  will have the same surface temperature as a flat terrain consisting of the same material.* This is consistent with the derivation in Section 3.4, showing that when  $A = 0$ , a concave spherical segment is no different from a flat terrain. This is because  $\chi = \xi$  for that particular geometry. However, for many terrains  $\chi \neq \xi$  and according to Eq. (58) we cannot expect their temperature to reach that of a flat surface even when  $D \ll L$  and all lateral temperature gradients are removed.

We now proceed to demonstrate excellent agreement between these analytical results and 3D heat conduction simulations for various types of irregular terrains.

## 4. Results

We here discuss remaining lateral temperature gradients in 3D heat conduction models (Section 4.1), and verify numerically that various topographies behave thermally as if flat as long as  $\chi = \xi$  and  $A = 0$  (Section 4.2), but that discrepancies are found for concave spherical segments when  $A > 0$  (Section 4.3), and for a number of different topographies when  $\chi \neq \xi$  (Sections 4.4 and 4.5). We finally discuss a convex spherical segment surrounded by an infinite flat plain (Section 4.6).

### 4.1. Temperature dispersion on surfaces with small-scale roughness

A rough terrain tends to develop a surface temperature dispersion due to variations in surface slope with respect to the solar direction, shadow formation and self heating by scattered solar radiation and thermal emission. This temperature dispersion can become strong when the size scale  $D$  of topographic features is large compared to the thermal skin depth  $L$ . However, when  $D \lesssim L$ , three-dimensional heat conduction tends to smooth out the temperature dispersion by efficiently conducting energy from hot to cold regions. Thereby, a rough terrain may be quasi-isothermal at any given instant during the diurnal cycle.

To illustrate these principles, we consider the concave spherical segment seen in the upper left panel of Fig. 1 and described in the caption of Table 3. We assume  $A = 0$  and  $\varepsilon = 1$ . The density  $\rho$ , specific heat capacity  $c$  and heat conductivity  $\kappa$  are taken to be  $\rho = 3600 \text{ kg m}^{-3}$ ,  $c = 830 \text{ J kg}^{-1} \text{ K}^{-1}$ , and  $\kappa = 0.4694 \text{ W m}^{-1} \text{ K}^{-1}$ , values that are relevant for solid rock. The density is intermediate between forsterite and fayalite (Horai, 1971), the specific heat capacity is close to that of forsterite at  $T = 290 \text{ K}$  (Robie et al., 1982), and the heat conductivity is an order of magnitude lower than that of olivine (Horai, 1971) to account for the presence of cracks. This yields a thermal inertia  $\Gamma = \sqrt{\rho c \kappa} = 1184 \text{ J m}^{-2} \text{ K}^{-1} \text{ s}^{-1/2} = 1184 \text{ MKS}$ . Applying a rotational period of  $P = 160 \text{ h}$  yields a thermal skin depth of  $L = \sqrt{\kappa/\rho c \omega} = 0.12 \text{ m}$ , which means that the diurnal surface temperature variation is damped by a factor  $e^{-1}$  at this depth, or to  $\sim 37\%$  of the surface

value. Efficient thermal communication between two regions therefore requires that the distance between them is at most a decimeter. The spherical segment under consideration has a diameter of  $0.036 \text{ m}$ , i.e.,  $D = 0.3L$ . The long rotation period was selected to make  $L$  larger than  $D$ . An even larger skin depth would have been better (since we strive for  $D \ll L$ ), but it must be kept in mind that the slab under the surface needs to have a thickness of several skin depths, to be consistent with our model assumption of a negligible vertical heat flux across the bottom of the domain. Furthermore, accurate solutions require that each skin depth is resolved by a sufficiently large number of grid cells. Here, each skin depth is resolved by 60 cells, which is more than necessary, the reason being that the crater geometry needs to be sufficiently resolved. In the current simulations, the domain extends  $0.8 \text{ m}$  under the crater floor ( $\sim 7L$ ), and more than  $1.6 \times 10^5$  grid cells are used. A larger skin depth would have become too computationally costly, and we demonstrate below that the remaining temperature dispersion is small enough for our purposes.

The crater is placed at the equator of a body located  $1 \text{ AU}$  from the Sun, having a spin axis that is perpendicular to the orbital plane. In order to demonstrate the importance of three-dimensional heat conduction in the current example, we here compare a 3D simulation with a 1D simulation (heat only flowing vertically). Fig. 4 shows the surface temperature distribution for the 1D version (left) and 3D version (right) at two different instances; midways between sunrise and noon ( $t = 60 \text{ h}$ ) in the upper panels, and at noon ( $t = 80 \text{ h}$ ) in the lower panels. The surface temperature of the forenoon 1D model clearly shows the effect of shadows ( $\min(T) = 221.6 \text{ K}$ ) as well as of small incidence angles and self heating ( $\max(T) = 384.7 \text{ K}$ ), values that should be compared to the temperature of flat terrain,  $314.2 \text{ K}$ . Due to the rapid surge in solar intensity during sunrise, the 3D model does not quite manage to smooth out temperature gradients ( $\min(T) = 296.6 \text{ K}$  and  $\max(T) = 328.3 \text{ K}$ ), but the range of temperature ( $\Delta T = \max(T) - \min(T) = 31.7 \text{ K}$ ) is substantially smaller than for the 1D case ( $\Delta T = 163.1 \text{ K}$ ).

At noon, illumination comes straight from above, but the 1D crater still has relatively cool ( $\min(T) = 334.2 \text{ K}$ ) and warm ( $\max(T) = 386.6 \text{ K}$ ) regions since the surface remembers the previous illumination history due to the high thermal inertia. Since the illumination flux changes less rapidly near noon compared to the forenoon, the 3D model can smooth out temperature gradients more efficiently ( $\min(T) = 366.7 \text{ K}$  and  $\max(T) = 370.0 \text{ K}$ ). Compared to the 1D model ( $\Delta T = 52.4 \text{ K}$ ), the 3D model has a small temperature dispersion at noon, only  $\Delta T = 3.3 \text{ K}$ .

The upper panel of Fig. 5 shows the mean surface temperature of the 3D terrain (circles) during different instances of the day, with bars indicating the standard deviation  $\sigma_T$  as a measure of temperature dispersion. The  $\sigma_T$  is particularly small near noon and during nighttime, and in spite of a higher  $\sigma_T$  during sunrise and sunset, the dispersion is always small compared to the temperature variation during the diurnal cycle. Therefore, the 3D model is *quasi-isothermal* at any given moment.

### 4.2. Surfaces with $\chi \approx \xi$ and with zero albedo

How does the temperature of the momentarily quasi-isothermal rough terrain compare to that of a flat terrain consisting of the same material? Because the roughness is due to concave spherical segments, and because the material has  $A = 0$  and  $\varepsilon = 1$ , we expect to find exactly the same temperature, based on the discussion in Section 3.4. This is consistent with Eq. (58) in Section 3.5 since  $\chi = \chi_p = 0.18159$  and  $\xi = 0.17869$  for the terrain in Section 4.1 (i.e.,  $\chi$  and  $\xi$  differ by merely  $1.6\%$ ). To test the prediction of the analytical derivation, we here perform a simulation with a 1D thermophysical model, developed to study flat surfaces.



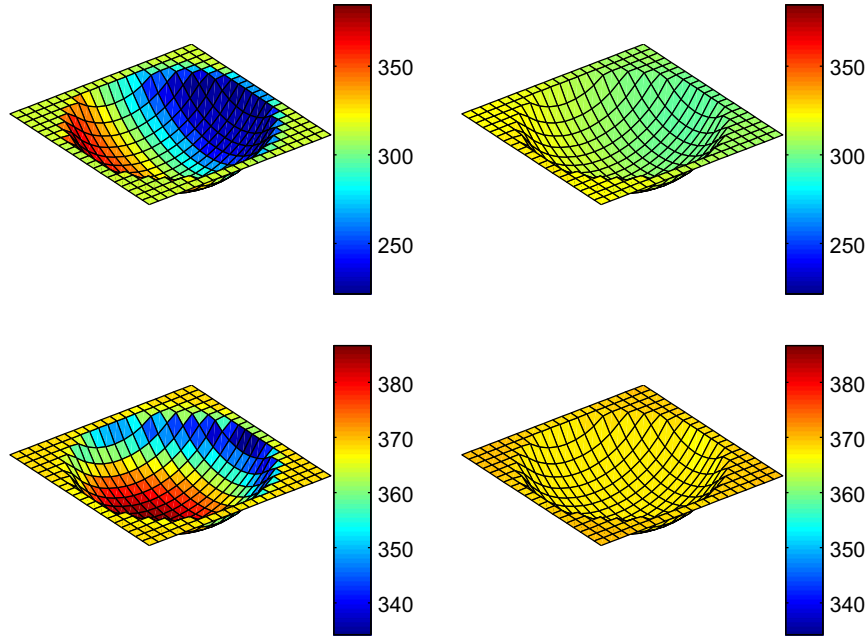


**Fig. 4.** Left panels: the surface temperature distribution for 1D vertical heat conduction for a  $P = 160$  h body at  $t = 60$  h (upper panel) and at  $t = 80$  h (lower panel). Right panels: the surface temperature distribution for 3D heat conduction for a  $P = 160$  h body at  $t = 60$  h (upper panel) and at  $t = 80$  h (lower panel). In both cases, the terrain has cross section  $4 \times 4$  cm<sup>2</sup> and is modeled to a depth of 80 cm. See Table 3 and Section 4.1 for further details.

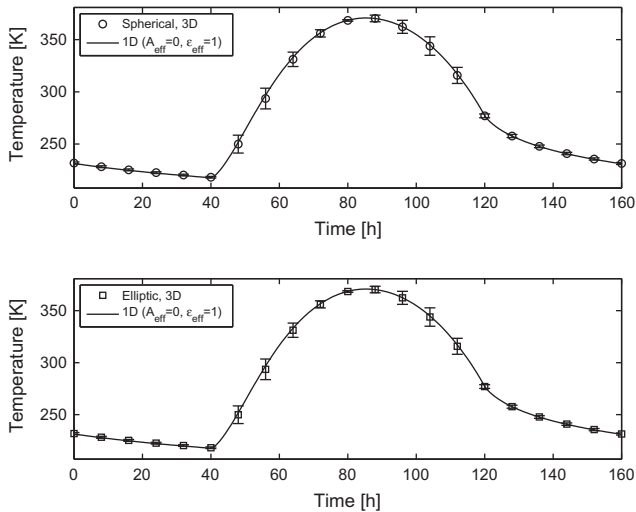


**Fig. 5.** Upper panel: the solid curve shows the surface temperature of a flat equatorial area on a body placed at 1 AU, and having its rotation axis perpendicular to the orbital plane. The rotational period is  $P = 160$  h and the thermal inertia is  $I^* = 1184$  MKS. The circles show the average surface temperature of a  $4 \times 4$  cm<sup>2</sup> patch containing a  $h = 1.08$  cm deep crater with rim radius  $R_{\text{rim}} = 1.8$  cm, with all other parameters as above (see upper left panel of Fig. 1 for topography). The error bars show the standard deviation  $\sigma_T$  of the surface temperature of the crater at any given moment. Lower panel: a corresponding plot for a concave oblate ellipsoidal segment (see upper right panel of Fig. 1).

We emphasize that this simulation, and all other 1D simulations in the remainder of the paper, have been done with a separate code, using a numerical scheme (the finite element method), that is very different from that of the 3D code. Therefore, we here not only verify the correctness of the analytical derivations with these numerical experiments, we also demonstrate that the 3D code has been implemented correctly. The result of the 1D model run for  $A_{\text{eff}} = 0$  and  $\epsilon_{\text{eff}} = 1$  is seen in the upper panel of Fig. 5 as a solid curve. The match with the

3D simulation is excellent and verifies that a cratered surface is *indistinguishable* from a flat one, as long as the craters are shaped as spherical segments, are non-scattering, and small compared to the thermal skin depth. This lends support to the common assumption that the effects of small-scale roughness can be ignored and that 1D heat conduction is sufficient when studying the effects of large-scale roughness.

The similarity in temperature between flat and non-flat terrains is not restricted to concave spherical segments. As an example, we considered a crater shaped as a *concave oblate ellipsoid segment*, seen in the upper right panel of Fig. 1. The numerical representation of the crater has  $\xi = 0.1747$  and  $\chi = 0.1796$ , i.e., they differ by merely 2.8%. We have reason to believe that this small difference may be caused by the finite resolution (for example, the spherical segment had a 1.6% difference between  $\chi$  and  $\xi$  for 800 facets, that was reduced to 0.7% for 7200 facets). From Eq. (58) we expect this topography to be thermally indistinguishable from a flat surface as well, since  $\chi \approx \xi$ . The mean temperature of this terrain according to the 3D model is shown (squares) as function of time in the lower panel of Fig. 5. Indeed, the solution is identical to the flat 1D model with  $\{A, \epsilon\} = \{0, 1\}$ , represented by the solid curve.

A third example is provided by the highly irregular negative relief random Gaussian terrain seen in the lower left panel of Fig. 1, for which  $\{\chi, \xi\} = \{0.32301, 0.30091\}$ . Fig. 6 shows that the 1D and 3D solutions generally follow each other closely, with some minor discrepancies for reasons seen in Fig. 3. The actual absorption of solar energy follows the asterisks in that figure, while the 1D model assumes a perfectly sinusoidal function. However, it is clear that there are no serious discrepancies.

We emphasize that the equality between these rough 3D models with  $D \ll L$  and flat 1D models only is valid since we consider  $A = 0$  and  $\chi = \xi$ . In the next section, we demonstrate that the temperatures are different for strongly scattering material, even when the topography is that of a concave spherical segment. We also investigate the limitations of the single-scattering assumption.

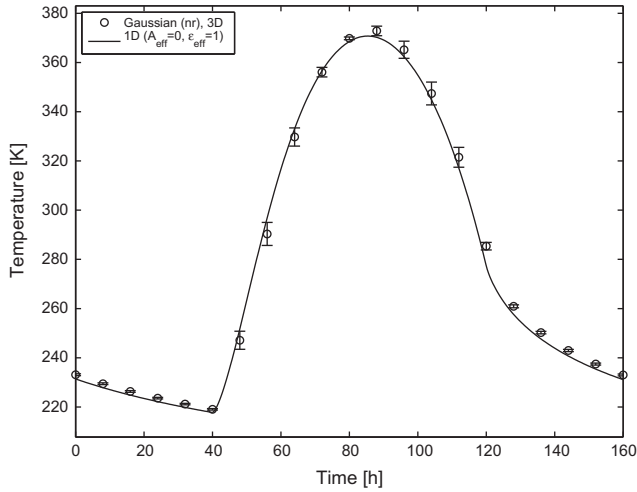


**Fig. 6.** The average surface temperature of the negative relief (nr) random Gaussian terrain seen in the lower left panel of Fig. 1 according to the 3D model (circles, with error bars indicating the standard deviation  $\sigma_T$  of the surface temperature), compared to the temperature of a smooth surface (solid curve). In both cases,  $\Gamma = 1184$  MKS,  $\mathcal{P} = 160$  h, and  $r_h = 1$  AU. The terrains are located at the equator of an object with spin axis perpendicular to the orbital plane.

#### 4.3. A strongly reflecting concave spherical segment

According to Table 3, based on Eq. (45), the equality between  $\{A_{\text{eff}}^{\text{ms}}, \epsilon_{\text{eff}}^{\text{ms}}\}$  and  $\{A, \epsilon = 1 - A\}$  gradually breaks down as  $A$  increases. The consequence of this must be that a spherical segment crater consisting of a certain material characterized by  $\{A, \epsilon\}$ , no longer will have the same temperature as a flat terrain consisting of the same material. However, it should be possible to *mimic* the temperature of the rough terrain with a 1D model, as long as that model is evaluated for  $\{A_{\text{eff}}^{\text{ms}}, \epsilon_{\text{eff}}^{\text{ms}}\}$ .

These principles are illustrated in Fig. 7. A highly reflecting material with  $A = 0.8$  and  $\epsilon = 0.2$  is considered. According to the 1D model, a flat surface will have a time-dependent temperature as given by the solid curve. When the 3D model is run with the same material parameters  $\{A, \epsilon\} = \{0.8, 0.2\}$ , quasi-isothermal solutions are obtained at different instances of time, with averages indicated by the squares. It is clear that the rough terrain has lower nighttime temperatures and higher daytime temperatures than the 1D model. Qualitatively, the rough terrain behaves as if it had a lower thermal inertia than the flat terrain. The differences are rather small, at most  $\sim 4$  K, but the standard deviation of the surface temperature dispersion on the rough terrain is even smaller. Thus, the difference between the rough and the flat surfaces is significant, in the mathematical sense.

According to Eq. (45) and Table 3, the 1D model should be able to reproduce the temperatures of the 3D model, as long as the albedo and emissivity are changed to their effective values,  $A_{\text{eff}}^{\text{ms}} = 0.76724$  and  $\epsilon_{\text{eff}}^{\text{ms}} = 0.23277$ . If the 1D model is run with these parameters, the dashed curve is obtained, which reproduces the 3D model perfectly.

This result is principally important since it challenges an assumption that always has been made by thermophysics modelers in planetary astronomy – that the level of roughness on “small” size scales has no influence on the thermal properties of the surfaces of atmosphereless Solar System bodies. The underlying reason for the 1D and 3D discrepancy developing at high Bond albedo is that identical temperatures no longer can be expected when  $\chi_p$  differs from  $\chi$ .

At this high level of reflectivity, when up to 80% of the downwelling solar photons will scatter at least once, one cannot expect

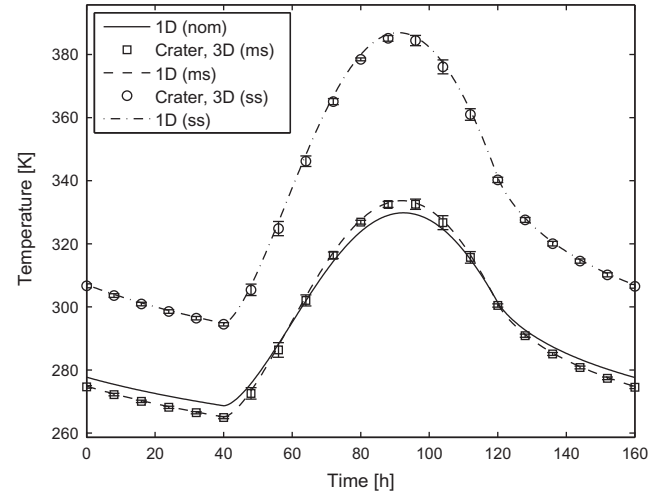


**Fig. 7.** A smooth surface with  $A = 0.8$ ,  $\epsilon = 0.2$ , and  $\Gamma = 1184$  MKS, located at the equator of a body with spin axis perpendicular to the orbital plane,  $\mathcal{P} = 160$  h, and  $r_h = 1$  AU has a surface temperature given by the solid curve. A 3D model with a  $h = 1.08$  cm spherical segment crater with rim radius  $R_{\text{rim}} = 1.8$  cm on a  $4 \times 4$  cm<sup>2</sup> patch, with multiple scattering accounted for has an average surface temperature shown by the squares. A 1D model run with  $A_{\text{eff}}^{\text{ms}} = 0.76724$  and  $\epsilon_{\text{eff}}^{\text{ms}} = 0.23277$  (see Eq. (45) and Table 3) yields the dashed curve that coincides with the 3D model. If the 3D model is run with the single scattering assumption, the average surface temperatures given by the circles are obtained. These temperatures can be reproduced by a 1D model when using  $\{A_{\text{eff}}^{\text{ss}}, \epsilon_{\text{eff}}^{\text{ss}}\} = \{0.66518, 0.19929\}$  (see Table 3).

that a single scattering assumption will result in realistic temperatures. The single scattering assumption basically makes the surface more “sticky” to radiation, since a scattered photon will be absorbed with certainty, if it ever interacts with the surface material again. Hence, a strong elevation of the temperature is expected, compared to multiple-scattering simulations. This is evident when the 3D code is run in single scattering mode – the circles in Fig. 7 are displaced upward by up to 53 K with respect to the multiple-scattering data.

In Section 3.4 we demonstrated that the single scattering assumption could be accounted for by replacing  $\chi_{p,\text{crat}}$  by  $\xi_{\text{crat}}$  in the expressions for  $\{A_{\text{eff}}^{\text{ms}}, \epsilon_{\text{eff}}^{\text{ms}}\}$ , thereby obtaining Eq. (46). If the 1D model is run for the parameter pair  $\{A_{\text{eff}}^{\text{ss}}, \epsilon_{\text{eff}}^{\text{ss}}\} = \{0.66518, 0.19929\}$  (see Table 3) we obtain the dashed-dotted curve, that is in excellent agreement with the 3D model when run in single scattering mode. This illustrates that the underlying mechanisms and principles of the physics and assumptions involved are well understood. We are therefore confident that a comparison between  $\{A_{\text{eff}}^{\text{ms}}, \epsilon_{\text{eff}}^{\text{ms}}\}$  and  $\{A_{\text{eff}}^{\text{ss}}, \epsilon_{\text{eff}}^{\text{ss}}\}$  given by Eqs. (45) and (46) accurately shows under what conditions the single scattering assumption is sufficiently accurate.

Fig. 8 shows  $A_{\text{eff}}^{\text{ms}}$  and  $A_{\text{eff}}^{\text{ss}}$  versus  $A$  in the upper panel and  $\epsilon_{\text{eff}}^{\text{ms}}$  and  $\epsilon_{\text{eff}}^{\text{ss}}$  versus  $\epsilon$  in the lower panel. Also  $A$  and  $\epsilon$  are plotted in the upper and lower panels, respectively, to highlight differences and similarities with respect to the corresponding multiple and single scattering quantities. Note that  $\epsilon_{\text{eff}}^{\text{ss}}$  and  $\epsilon$  are practically indistinguishable, as discussed in Section 3.4. As expected, the difference between the single and multiple scattering versions of the effective albedo and emissivity are small when the material albedo is small. However, the discrepancies grow steadily when  $A$  increases. At  $A = 0.8$ , the difference between  $A_{\text{eff}}^{\text{ss}}$  and  $A_{\text{eff}}^{\text{ms}}$  amounts to 13.3% while the difference between  $\epsilon_{\text{eff}}^{\text{ss}}$  and  $\epsilon_{\text{eff}}^{\text{ms}}$  is 14.4%. As can be seen in Fig. 7, such discrepancies lead to errors in temperature of up to 53 K. At  $A = 0.27$ , the differences between single and multiple scattering versions of effective albedos and emissivities are down to 5% and the largest difference in temperature during day or night is 5.8 K. At

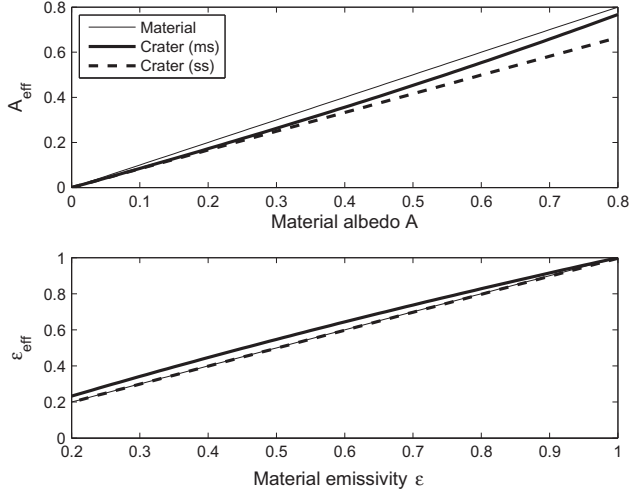


**Fig. 8.** Upper panel: bond albedo for the concave spherical segment described in Table 3 assuming multiple scattering ( $A_{\text{eff}}^{\text{ms}}$ ) or single scattering ( $A_{\text{eff}}^{\text{ss}}$ ) as functions of the material Bond albedo  $A$  (see Eqs. (45) and (46)). Lower panel: the corresponding emissivities.

$A = 0.15$  the corresponding numbers are 3% and 2.9 K, and at  $A = 0.04$  we have 1% and 0.9 K. All these numbers apply for the currently considered topography, heliocentric distance, spin axis and latitude. Therefore, the single scattering approximation should be reasonably valid when working with, e.g., comets ( $A \sim 0.04$ ) and asteroids ( $A \lesssim 0.25$ ), but not when considering bright icy satellites, saturnian ring particles *et cetera*.

#### 4.4. A sinusoidal trench terrain with zero albedo

So far, all considered terrains had  $\chi = \xi$ , purely based on their geometric properties, being indistinguishable from a flat one when  $A = 0$  and  $\varepsilon = 1$  (since  $\chi_p = \chi = \xi$ , causing Eq. (45) to yield  $A_{\text{eff}}^{\text{ms}} = 0$  and  $\varepsilon_{\text{eff}}^{\text{ms}} = 1$ ). The concave spherical segment with  $A > 0$  and  $\varepsilon < 1$  proved to differ from a flat surface of the same material (ultimately because  $\chi_p \neq \chi$ ), in a manner consistent with predictions from Eq. (45) in the multiple scattering scenario, and from Eq. (46) in the single scattering scenario.

We now proceed to cases with  $\chi \neq \xi$ . According to the discussion in Section 3.5, such rough terrains will have temperatures differing from that of flat surfaces even when  $A = 0$ , according to Eq. (58). The lower right panel of Fig. 1 shows a terrain consisting of three roughly sinusoidally shaped trenches. The level of roughness is described by  $\theta = 34.3^\circ$  and  $s_{\text{rms}} = 44.2^\circ$ , and is similar to the  $s_{\text{rms}} = 43^\circ$  roughness level successfully applied by Spencer (1990) for Asteroid (1) Ceres. The small scale roughness parameter for this terrain is  $\xi = 0.30989$ , but the small scale self heating parameter based on view factors is merely  $\chi = 0.24997$ . This amounts to a difference of almost 20%, i.e., is rather substantial.

The results of the 3D heat conduction simulations ( $A = 0$  and  $\varepsilon = 1$  for the surface material) are shown in Fig. 9 as circles with error bars showing  $\sigma_T$ . When the 1D model is run for the same material parameters, without any form of correction, the solid curve is obtained. The rough terrain is systematically cooler than the flat terrain, by up to 9 K. The difference is significant in the sense that  $\sigma_T$  at any given moment is substantially smaller than the difference between the models. The dashed curve shows the 1D solution according to Eq. (58) with the correction factor  $(1 - \chi)/(1 - \xi) = 1.0868$ , and is consistent with the 3D model.

We note that the view factors and  $\chi$ -value, as well as the temperature distribution across the surface versus time in the limit of zero thermal inertia are *identical* when comparing our simulations

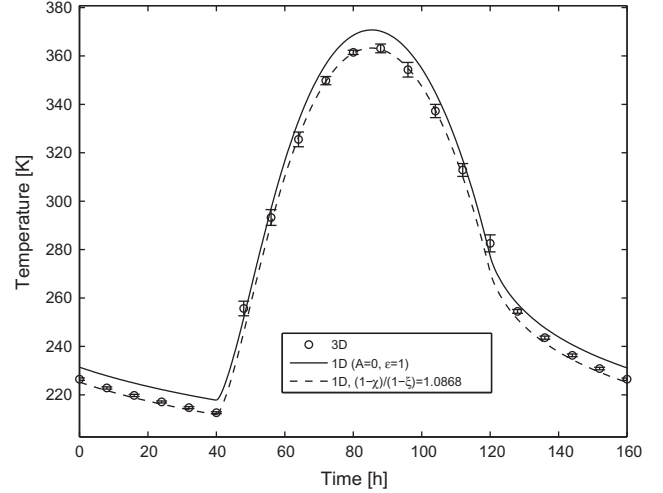


**Fig. 9.** The solid curve shows the diurnal temperature of a flat terrain, evaluated with a standard 1D model with  $\{A, \varepsilon\} = \{0, 1\}$ . The circles show the average temperature of the 3D model for a sinusoidal trench terrain ( $\theta = 34.3^\circ$ ,  $s_{\text{rms}} = 44.2^\circ$ ,  $\chi = 0.24997$ ,  $\xi = 0.30989$ ). These average temperatures can be reproduced by a 1D model evaluated for  $(1 - \chi)/(1 - \xi) = 1.0868$  (dashed) according to Eq. (58).

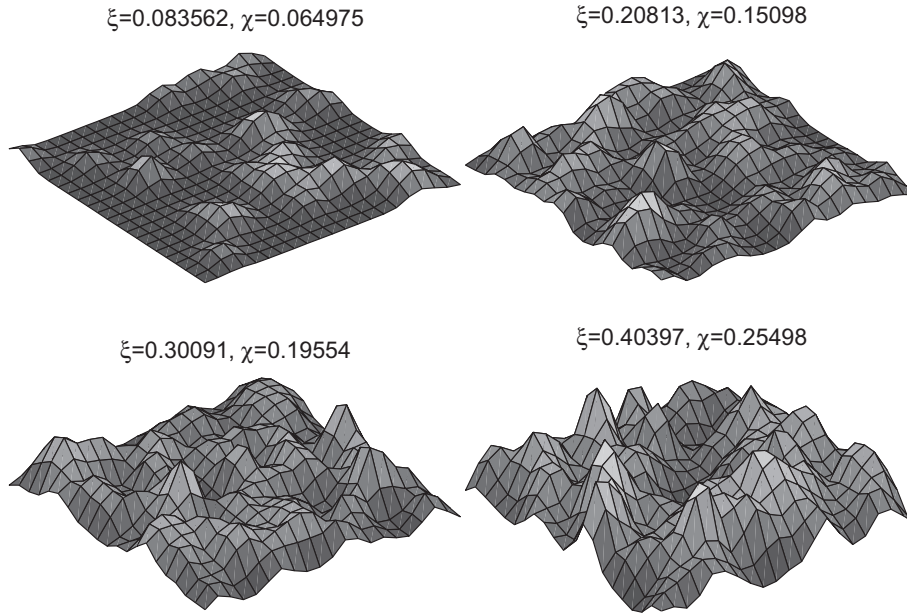
to the model presented by Gutiérrez et al. (2001). Therefore, we have no reason to doubt our simulations.

#### 4.5. Positive relief random Gaussians with zero albedo

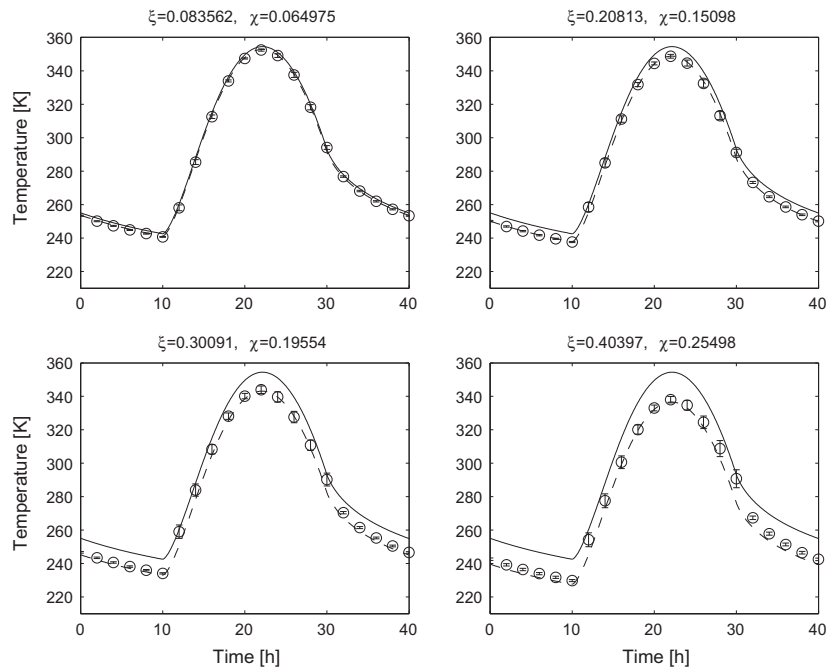
We now proceed to study another type of surface, also characterized by  $\chi \neq \xi$ . Fig. 10 shows a suite of increasingly rough terrains, created by randomly placing convex Gaussians on initially flat terrains (creating positive relief). As shown in Fig. 10, the small scale roughness parameter here has a range of  $0.08 \lesssim \xi \lesssim 0.40$  while the small scale self heating parameter based on view factors  $\chi$  is systematically smaller,  $0.06 \lesssim \chi \lesssim 0.25$ . The difference between  $\xi$  and  $\chi$  increases with the level of roughness.

Fig. 11 shows the corresponding 3D surface temperature averages as circles. In the current simulations,  $\rho = 3600 \text{ kg m}^{-3}$ ,  $c = 830 \text{ J kg}^{-1} \text{ K}^{-1}$ , and  $\kappa = 0.4694 \text{ W m}^{-1} \text{ K}^{-1}$  as before, but the rotational period is reduced to  $\mathcal{P} = 40 \text{ h}$ . Thus, the thermal skin depth  $L = 0.06 \text{ m}$  is reduced to half compared to the previous simulations (the domain thickness is  $0.4 \text{ m}$  and the number of volumetric cells is  $8.1 \times 10^4$ ). However, the surface temperature dispersion remains small, since the size of topographical features typically are smaller than in previous simulations. As seen in Fig. 11, the standard deviation is typically smaller than the circular symbols used for the plotting. All model runs used  $\{A, \varepsilon\} = \{0, 1\}$  and are compared to the flat-surface 1D solution (solid curves), evaluated for the same Bond albedo and emissivity. The 3D model temperatures are systematically lowered with respect to the 1D model, when  $\xi$  is increasing. The mean differences between the flat-surface 1D and average 3D temperatures are 1.8 K, 4.8 K, 7.9 K, and 12.4 K for  $\xi = 0.08$ ,  $\xi = 0.20$ ,  $\xi = 0.30$ , and  $\xi = 0.4$ , respectively.

The dashed curves show solutions to Eq. (58), with  $(1 - \chi)/(1 - \xi)$  taking the values 1.0203, 1.0722, 1.1507, and 1.2499, as  $\xi$  increases. These corrected 1D models are indeed similar to the 3D models. The mean differences between the corrected 1D solutions and the average 3D temperatures are 0.5 K, 0.7 K, 2.4 K, and 3.8 K, in order of increasing surface roughness. The largest discrepancies are found on the early morning and late evening parts of the temperature curve. The reason for these discrepancies can be seen in Fig. 3, that shows the illumination



**Fig. 10.** Four positive relief random Gaussian terrains, having different small scale roughness parameters  $\xi$  that differ from the small scale self heating parameter  $\chi$  as indicated in the figure. Upper left surface has  $\bar{\theta} = 13.6^\circ$  and  $s_{rms} = 22.5^\circ$ , upper right surface has  $\bar{\theta} = 23.6^\circ$  and  $s_{rms} = 35.5^\circ$ , lower left surface has  $\bar{\theta} = 30.9^\circ$  and  $s_{rms} = 42.9^\circ$ , lower right surface has  $\bar{\theta} = 38.6^\circ$  and  $s_{rms} = 50.0^\circ$ .



**Fig. 11.** The average temperatures of the terrains in Fig. 10 according to the 3D model (circles) with  $\Gamma = 1184$  MKS,  $P = 40$  h, and  $r_h = 1$  AU, assuming a location at the equator of a body with spin axis perpendicular to the orbital plane. The temperatures are lower than those expected for a smooth surface (solid curve), and the difference increases with  $\xi$ . A 1D model can reproduce the temperatures (dashed) by adjusting the emissivity according to Eq. (58), with small discrepancies caused by the approximation made in Eq. (53).

conditions for the  $\xi = 0.30$  positive relief random Gaussian terrain as circles. It is clear that the positive relief of these terrains allow illuminated peaks to collect more radiation at high solar incidence angles, than a flat surface, for which the power changes as  $(1 - \xi)\mu$ . Because this simplified expression is used by the 1D models (dashed), these become somewhat cooler than the corresponding 3D models.

Why are sinusoidal trench terrains and certain random Gaussian terrains systematically cooler than, e.g., concave spherical seg-

ments and flat surfaces? The physical interpretation of these results is that the absorbed solar power (proportional to the cross section turned towards the Sun,  $\mu S_{flat}$ ) is smeared out over the entire surface area of the rough terrain  $S_{rough}$ , leading to rather low temperatures and levels of emission. This temperature reduction is counteracted by self heating. For some topographies, this mechanism manages to bring the temperature fully up to that of a flat terrain, as long as no scattering takes place. However, when  $\chi < \xi$  the self heating is incapable of doing so, even when  $A = 0$ .



That is to say, energy conservation is valid, and  $P_{\text{abs}} = P_{\text{out}} = P_{\text{prod}} - P_{\text{sh}}$  holds (when integrated over a rotational period), but  $P_{\text{prod}}$  is too low compared to a flat surface since  $P_{\text{sh}}$  is not sufficiently high. Mathematically, the effect is the same as if executing a standard 1D thermophysical model with a non-physical emissivity, taking a value above unity.

The difference between the 1D and 3D solutions for the  $\xi = 0.30$  surface seen in the lower left panel of Fig. 10 is particularly interesting. This is because the irregular terrain discussed at the end of Section 3.5, seen in the lower left panel of Fig. 1, was obtained simply by *mirroring* the current  $\xi = 0.30$  surface in the  $\hat{x}$ - $\hat{y}$ -plane. The currently considered terrain with  $\chi < \xi$  has positive relief and becomes cooler than a flat surface with the same average orientation and illumination history. Also the parallel sinusoidal trench terrain has positive relief,  $\chi < \xi$ , and is cooler than a flat surface. However, the random Gaussian terrain in Section 3.5 has negative relief,  $\chi = \xi$ , and developed a temperature that did not differ substantially from that of the 1D model, according to Fig. 6. It therefore behaves as the concave spherical and ellipsoid segments, that also have negative relief. The question is then why surfaces with positive relief behave so differently compared to those with negative relief.

The answer is that the radiation smearing experienced by a single topographical feature can be compensated for through self heating by *the feature itself* when it is concave. However, when the feature is convex, it must rely on *exterior* surfaces in order to receive the correct dose of self heating. This may be achieved as long as the convex feature is part of a negative relief, but not necessarily if the relief is positive. In the following, this is illustrated by a simple example – a convex spherical segment located on an infinite flat plain.

#### 4.6. The convex spherical segment

Consider an isolated convex spherical segment with height  $h$  and curvature radius  $R$ . The small scale roughness parameter is then equal to the height to curvature diameter ratio  $S$ , i.e.,  $\xi = S = h/2R$ . For example, a hemispherical segment has the largest possible value,  $\xi = 1 - S_{\text{flat}}/S_{\text{rough}} = 1 - \pi R^2/2\pi R^2 = 1/2$ . However, due to the convex shape, the angle between an outward surface normal at a specific surface location, and the direction vector to any other surface location, will always exceed  $90^\circ$ . Hence, all view factors are zero, and there is no self heating. With  $\xi \leq 0.5$  and  $\chi = 0$ , the isolated convex spherical segment smears the absorbed solar radiation over a large surface area without *any* compensating self illumination and becomes rather cold.

When a spherical segment with  $A = 0$  and  $\varepsilon = 1$  is illuminated from above by the solar flux  $F_\odot$ , and is heated or cooled from below by the heat conduction flux  $\mathcal{K}$  (taken positive if directed downwards), the net absorbed power is given by the net heating flux  $F_{\text{heat}} = F_\odot - \mathcal{K}$  times the flat area enclosed by the rim of the convex spherical segment, or  $P_{\text{heat}} = 4\pi R^2 S(1 - S)F_{\text{heat}}$ . The produced power equals the escaping power, and is obtained by multiplying the surface area of the convex spherical segment with the thermal emission flux evaluated for the surface temperature  $T_{\text{ss}}$  (the spherical segment is assumed isothermal due to efficient heat conduction),  $P_{\text{prod}} = P_{\text{out}} = 4\pi R^2 S\sigma T_{\text{ss}}^4$ . Balancing  $P_{\text{heat}}$  and  $P_{\text{out}}$ , while remembering that a flat terrain has  $F_\odot = \sigma T_{\text{flat}}^4 + \mathcal{K}$  yields

$$T_{\text{ss}} = (1 - S)^{1/4} T_{\text{flat}}, \quad (59)$$

which is as low as  $T_{\text{ss}} = 252$  K for a hemispherical segment with  $S = 0.5$  if  $T_{\text{flat}} = 300$  K.

In order for the spherical segment to reach  $T_{\text{flat}}$ , it must receive power in addition to solar radiation and conduction, i.e., it must be surrounded by terrain that illuminates it by thermal radiation. Spec-

cifically, the power produced by the spherical segment under such conditions  $P_{\text{prod}} = 4\pi R^2 S\sigma T_{\text{flat}}^4 = 4\pi R^2 S F_{\text{heat}}$  must be balanced by a combination of solar irradiance, heat conduction and thermal illumination  $P_{\text{heat}} + P_{\text{sh}} = 4\pi R^2 S(1 - S)F_{\text{heat}} + P_{\text{sh}}$ , which only is possible if

$$P_{\text{sh}} = 4\pi R^2 S^2 F_{\text{heat}} = \pi h^2 F_{\text{heat}}. \quad (60)$$

We here explore the most simple form of surrounding terrain – an infinite flat plain. The purpose is to investigate whether such an environment with temperature  $T_{\text{flat}}$  can provide the power  $P_{\text{sh}}$  needed to give the spherical segment the temperature  $T_{\text{flat}}$  as well.

Thus, consider a small area element  $j$  located on the spherical segment. According to Eq. (22) and item #2 discussed in Section 3.1, facet  $j$  is illuminated by the flux  $F_{\text{heat}} \mathcal{F}_{jk}$  originating from a facet  $k$  with surface area  $S_k = dxdy$  located on the flat plain, which coincides with the  $\hat{x}$ - $\hat{y}$ -plane. The total self heating flux at  $j$  is thus obtained by adding up all contributions from plain facets,

$$F_{\text{heat}} \sum_{k \neq j} \mathcal{F}_{jk} = F_{\text{heat}} \int_{y_{\min}}^{y_{\max}} \int_{x_{\min}}^{x_{\max}} \frac{\cos \theta_j \cos \theta_k}{\pi r^2} dxdy. \quad (61)$$

To perform the integration, it is necessary to specify the integrand and integration limits as function of  $x$  and  $y$ . Without loss of generality due to symmetry reasons, we may consider a  $j$  facet located in the  $\hat{y}$ - $\hat{z}$ -plane. By considering the position and normal vector of a random facet  $k$  on the plain we evaluate the integrand and integration limits, and obtain the solution as follows,

$$\begin{aligned} F_{\text{heat}} \sum_{k \neq j} \mathcal{F}_{jk} &= \frac{F_{\text{heat}} \beta}{\pi R} \int_{y_{\min}}^{y_{\max}} \int_{-\infty}^{+\infty} \frac{y_j y - y_j - \beta \gamma}{(x^2 + (y - y_j)^2 + \beta^2)^2} dxdy \\ &= \frac{F_{\text{heat}}}{2} (1 - \sqrt{1 - (y_j/R)^2}) \end{aligned} \quad (62)$$

where auxiliary expressions are given by

$$\begin{cases} \beta = \sqrt{R^2 - y_j^2} + h - R \\ \gamma = R - h + \beta \\ y_{\min} = \frac{y_j^2 + \beta \gamma}{y_j} \\ y_{\max} = +\infty \end{cases} \quad (63)$$

In order to explore the contribution to the self heating flux at  $j$  from flat regions at different distances from the spherical segment,  $\mathcal{F}_{jk}$  was calculated for a terrain similar to the one seen in the upper left panel of Fig. 1, except that the current terrain is convex (curvature radius  $R = 0.02040$  m and height  $h = 0.01080$  m) and that the flat terrain had the dimensions  $0.12 \times 0.12$  m<sup>2</sup>, or about 5.9 curvature radii across. The total number of surface facets was 7200, compared to 800 used previously. A facet  $j$  was selected for study ( $y_j = 0.0107$  m), having a normal vector that tilted  $32.8^\circ$  with respect to  $\hat{n}_k$  (the largest slope on the terrain was  $57.2^\circ$ , located at the base of the spherical segment). Thus, facet  $j$  is roughly midways between the hill top and its base. By considering a gradually larger square centered on the spherical segment, and adding up the non-zero  $\mathcal{F}_{jk}$ -values, the dotted curve in Fig. 12 was obtained. It shows that the self heating flux grows steeply as the box size is increased, and is not leveling out at the edge of the considered domain ( $y_{\max} = 0.06$  m  $\approx 2.9R$ ). Since it was not practically feasible to consider a larger domain, Eq. (61) was integrated numerically, for an increasingly large quadratic domain. The result of this numerical integration is shown as a solid curve in Fig. 12. Due to the limited facet resolution when calculating  $\sum \mathcal{F}_{jk}$ , the agreement between the dotted and solid curves in the region of overlap is not perfect, but the differences are small, only about 5%. This makes us confident that both the view factors and the integral are correctly calculated, to within numerical errors. The solid curve should be compared with the dashed line, which is the analytical solution,

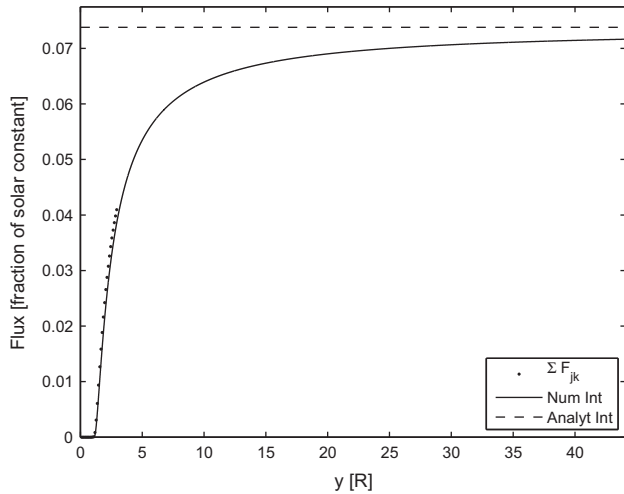


**Fig. 12.** In order to calculate the self heating flux of a facet located in a convex spherical segment, the contribution from surrounding flat terrain must be calculated. The solid curve shows the analytically calculated flux (according to numerical integration of Eq. (61)) for an increasingly large square of surrounding flat terrain. The curve asymptotically approaches the dashed line, which is the self heating flux from an infinitely large terrain according to Eq. (62). In order to verify the correctness of the integrand in Eq. (61), the flux is also calculated based on view factors (dotted), up to a domain size that is practically feasible to consider.

Eq. (62). As expected, the solid curve approaches the dashed line asymptotically. About 90% of the total self heating flux is provided by flat terrain located within 13 curvature radii from the spherical segment. Terrain beyond 40 curvature radii is responsible for several percent of the self heating flux. Thus, the spherical segment must rely on rather distant terrain for the illumination.

In order to calculate the total self heating power, Eq. (62) must be multiplied by the local surface area and integrated across the entire spherical segment. By using a spherical coordinate system (polar angle  $\vartheta$ , azimuth  $\phi$ ) with its origin at the center of the sphere of which the spherical segment is a cap, and recognizing that  $y_j = R \sin \vartheta$  the integral is given by

$$\begin{aligned}
 F_{\text{heat}} \sum_j \left( \sum_{k \neq j} \mathcal{F}_{jk} \right) s_j &= \frac{F_{\text{heat}}}{2} \int_0^{2\pi} \int_0^{\vartheta_{\text{max}}} \left( 1 - \sqrt{1 - \sin^2 \vartheta} \right) R^2 \\
 &\quad \times \sin \vartheta d\vartheta d\phi \\
 &= \pi R^2 F_{\text{heat}} \left[ \frac{1}{2} \cos^2 \vartheta - \cos \vartheta \right]_0^{\vartheta_{\text{max}}} \\
 &= \frac{1}{2} \pi h^2 F_{\text{heat}}, \quad (64)
 \end{aligned}$$

where the last step follows since the largest tilt has  $\cos \vartheta_{\text{max}} = (R - h)/R$ .

As can be seen, the power collected by a convex spherical segment from an infinite flat surrounding surface at temperature  $T_{\text{flat}}$  according to Eq. (64) is exactly half of the one needed to raise the temperature of the spherical segment to  $T_{\text{flat}}$  according to Eq. (60). Therefore, if sunlight, thermal infrared illumination, and heat conduction (at the same level as elsewhere) are the only sources of energy, the spherical segment will still be cooler than the surrounding plain.

However, there is a complicating factor. The spherical segment itself will emit thermal infrared radiation, of which some will illuminate the plain instead of escaping into space. With calculations similar to the ones above one can demonstrate that this power also equals  $\pi h^2 F_{\text{heat}}/2$ , if  $T_{\text{ss}} = T_{\text{flat}}$ . Therefore, the extra power given to the spherical segment is just returned back to the plain – a shuffling of energy between different parts of the terrain that does

not affect the net inflow or outflow of energy to the exterior, thus not violating global energy conservation. The only effect is that the surface temperature distribution is modified. Regarding the illumination of the plain, one can imagine two extreme scenarios.

1. All thermal flux absorbed by the plain is *conducted* back to the spherical segment (and add to  $\mathcal{K}$ ). Thus, the extra illumination of the plain does not modify its temperature. The spherical segment also reaches  $T_{\text{flat}}$  by a combination of solar illumination, thermal infrared self heating, and solid state heat conduction. Thus, the entire terrain has the temperature  $T_{\text{flat}}$  and is indistinguishable from a flat terrain, in spite of its topographical feature.
2. Flat terrain close to the spherical segment will reach a temperature above  $T_{\text{flat}}$  due to the extra illumination in addition to solar radiation. The elevated temperature means that the loss to space increases, and the difference between absorbed and lost fluxes will be given to the spherical segment as a combination of radiative self heating and solid state heat conduction. Since the spherical segment now misses out on a fraction of the energy, it will reach a temperature below  $T_{\text{flat}}$  (slightly reducing its own energy loss to space). Thus, the terrain will not be isothermal.

The key difference between the scenarios above is the solid state heat conductivity of the material. The first scenario in practice requires that heat conductivity is infinitely high so that thermal infrared flux, which has been absorbed by the plain arbitrarily far away from the spherical segment, can find its way back immediately. In other words, for realistic values of the heat conductivity, a convex spherical segment sitting on a flat plain will be cooler than  $T_{\text{flat}}$  while the plain will have a higher temperature, only approaching  $T_{\text{flat}}$  at infinity. The big difference between a negative and positive relief is that the former is capable of dealing with its large surface area (compared to its projected cross section) through a mechanism of increased emission and absorption that takes place within a *confined* geometrical region. Specifically, this region may have such a small physical size compared to the thermal skin depth that temperature gradients level out, and the terrain becomes thermally indistinguishable from a flat terrain. A terrain with positive relief is not capable of solving these problems within a small geometric region – it may have to involve terrain being located arbitrarily far away in the process. If that region is substantially larger than the thermal skin depth, the terrain will develop a lateral temperature gradient. Thereby, features smaller than the thermal skin depth may still cause significant deviations from the flat surface temperature, since its “thermal” size goes far beyond its physical size.

The terrain with negative relief seen in the lower right panel of Fig. 1 has  $\xi \approx \chi$ , is “self contained” and is therefore practically thermally indistinguishable from a flat terrain (Fig. 6). If this terrain is mirrored in the  $\hat{x}$ - $\hat{y}$ -plane, the resulting positive relief terrain has  $\chi < \xi$  and is not capable of reaching the temperature of a flat terrain. The internal self heating is not sufficient to compensate for the large surface area (compared to the cross section available for solar energy collection). In the current simulations, these problems are amplified by the fact that the terrains are *truncated* at a finite size, not being substantially larger than the features themselves. Convex features with positive relief near the boundary freely lose energy to space, and are not illuminated from the outside. This is an important reason for a lowered  $\chi$  value with respect to  $\xi$ , and the systematic difference in average temperature with respect to 1D simulations seen in Fig. 11. However, the previous discussion on the spherical segment indicates that this problem goes beyond mere numerical shortcomings. Even if a flat terrain was added exterior to the rough terrain, and even if it extended

$\sim 10$  times farther than current dimensions (increasing the number of surface facets by two orders of magnitude), it would still not close the gap between 1D and 3D models. This is not only due to remaining flux shortage on the  $\sim 10\%$  level, but also since the length scale of radiative transfer would exceed the thermal skin depth.

The 3D model mean temperature of a convex feature will be pushed towards the 1D model temperature if the surrounding flat plain is replaced by surface having a slightly concave shape – in practice creating an overall negative relief, containing a small local convexity. However, in reality it should be equally common that the surrounding terrain has a degree of overall convex curvature, i.e., a local convex feature sitting on a positive relief. For example, a roundish rock with a rough surface texture could represent such a global positive relief surface, with local convexities.

## 5. Discussion

We have used a novel thermophysical model to explore the effects of 3D heat conduction and roughness on size scales smaller than the thermal skin depth. Under certain conditions, the quasi-isothermal temperature of such a rough terrain becomes indistinguishable from that of a flat terrain. The requirements are that scattering of radiation does not take place, and that the small scale self heating parameter  $\chi$  equals the small scale roughness parameter  $\xi$ . Topographies that fulfill the latter criterion include concave spherical segments, concave oblate ellipsoidal segments, as well as negative relief random Gaussian terrains.

However, when these conditions were not met, we observed systematic deviations from the flat-surface temperature in numerical simulations, which could be reproduced in detail by analytical corrections to the Bond albedo and integrated hemispherical emissivity used in 1D models. First, the introduction of scattering on a rough terrain lowers the effective albedo and increases the effective emissivity, with respect to a flat surface consisting of the same material. The lowered albedo is due to an increased probability that a given photon will be absorbed, since it may interact with the surface numerous times while scattering about in concavities (see, e.g., Greenberg, 1986). The increased emissivity is just a consequence of the Kirchhoff law. A rough terrain will display a higher day-time temperature and a lower night-time temperature, than a flat terrain consisting of the same material.

Second, even non-scattering material with roughness may display a quasi-isothermal temperature different from that of a flat surface consisting of the same material, if  $\chi \neq \xi$ . We demonstrated the effect with 3D numerical simulations for sinusoidal trenches and positive relief random Gaussian. We could reproduce the results in detail with 1D simulations, for which the albedo, emissivity and heat conductivity had been adjusted analytically. It was possible to combine these corrections into a single modification of the emissivity in the form of an increase. As a result, terrains with  $\chi < \xi$  were systematically cooler than flat surface consisting of the same material. This is due to smearing of the absorbed radiation over a large surface area, and due to insufficient compensation by self heating. The effect is enhanced when the positive relief increases, and is optimized for isolated pieces of terrain, often considered in thermophysical models. Hence, it is not merely a numerical shortcoming in models without cyclic boundary conditions. Through analytical integration of view factors, we demonstrated that a convex spherical segment surrounded by an infinite flat surface – a proxy to a rock lying on smooth terrain – is expected to be cooler than its surroundings, even if the rock itself is smaller than the thermal skin depth. The flat ground near the rock will instead be hotter than flat regions further away.

We note that most workers in the field have assumed, explicitly or implicitly, that roughness on small scales has no effect on the thermophysical properties of the terrain under study. It has been taken for granted that the removal of surface temperature gradients by efficient lateral heat conduction simply restores the temperature of perfectly flat surfaces. This assumption is apparently not always true. In the following we comment on the consequences of this for remote sensing observations, as well as for lander missions and laboratory work.

The Bond albedo  $A_{\text{obs}}$  of minor Solar System bodies are routinely determined through combined optical and thermal infrared remote-sensing observations. This  $A_{\text{obs}}$  embodies the effects of atomic and mineralogical absorption as well as the effects of surface roughness on *all* size scales. If the level of surface roughness (e.g.,  $\bar{\theta}$  or  $s_{\text{rms}}$ ) is determined in the same process, it is important to realize that this roughness only applies to structures with  $D \gg L$ , i.e., size scales much larger than the skin depth. It is the strong lateral temperature gradients caused by shadows and self heating, that cannot be erased by lateral heat conduction, that are responsible for the spectral radiance alterations (with respect to a smooth body) that are observable in remote sensing. It is this alteration with respect to the ideal smooth case that allows  $\bar{\theta}$  or  $s_{\text{rms}}$  to be determined in the first place. Analogous to Eq. (45), the observed Bond albedo and the level of roughness can be used to reconstruct a higher Bond albedo, that is not affected by  $D \gg L$  roughness. In fact, this procedure is well-known, and has been described previously by, e.g., Lagerros (1998) and on page 67 in Mueller (2007). However, this corrected albedo is *not* necessarily the Bond albedo of the material itself (when forming a surface that is flat on size scales much larger than the wavelength). If the body has substantial  $D \ll L$  roughness, a further correction is needed according to Eq. (45) in order to remove the effects of small-scale roughness.

For example, assume that the Bond albedo is determined for flat and polished samples of HED meteorites in the laboratory. This Bond albedo should then be corrected for a potentially large degree of  $D \ll L$  roughness on the parent body, Asteroid (4) Vesta, before applying it as a Bond albedo for individual flat facets in a standard thermophysical model. This model, if accounting for large-scale roughness and multiple scattering, will automatically result in an effective Bond albedo that is also corrected for large-scale roughness. Adjustments of the level of large-scale roughness and thermal inertia in the model, when attempting to fit disk-integrated or resolved thermal infrared observations of Vesta, will then allow the determination of  $\bar{\theta}$  and  $\Gamma$  for Vesta. Without the small-scale roughness correction, the measured  $\bar{\theta}$  and  $\Gamma$  are distorted accordingly.

We have also found that surface patches of size  $\sim L$  may be cooler than expected, if they contain  $D \ll L$  roughness with prominent positive relief. This may be relevant for the interpretation of data from thermal infrared spectrometers carried by future landers or rovers, that may have  $\sim L$  resolution but not necessarily  $\ll L$  resolution. For example, there is a risk of misinterpreting temperature anomalies caused by small-scale surface roughness as due to albedo variegation.

Finally, we note that laboratory samples may have finite size and surface texture that result in  $\chi \neq \xi$ . If such samples are heated by illumination, and their thermal emission is observed, they will exhibit the temperature anomalies with respect to flat surfaces discussed in this paper. In order to correctly interpret the meaning of such observations, the effects discussed here should be taken into account.

## Acknowledgments

We are particularly grateful to Pedro J. Gutiérrez, who patiently has provided us simulations from his code, which allowed us to

verify the correctness of our own. This work has benefited substantially from discussions with Joshua L. Bandfield, Maria Teresa Capria, Joshua P. Emery, Olivier Groussin, Pedro J. Gutiérrez, Jörn Helbert, Laurent Jorda, Ekkehard Kürt, Alessandro Maturilli, Thomas G. Mueller, Ann L. Sprague, and Magdalena Wilska during Team meetings at the International Space Science Institute (ISSI) in Bern, Switzerland. We are grateful for the financial support of ISSI and for their generous hospitality during our Team meetings. We thank an anonymous referee for suggestions that substantially improved our manuscript, and we are grateful for the editorial work of Will Grundy. Davidsson also wishes to thank the Swedish National Space Board (SNSB) for financing contract 102/12. Rickman was supported by Grant Nr. 791/N-ROSJA/2010/0 of the Polish National Science Centre.

## References

- Bandfield, J.L., Hayne, P.O., Williams, J.-P., Paige, D.A., 2014. Lunar surface roughness derived from LRO Diviner Radiometer observations. *Icarus* (submitted for publication).
- Buhl, D., Welch, W.J., Rea, D.G., 1968a. Reradiation and thermal emission from illuminated craters on the lunar surface. *J. Geophys. Res.* 73 (16), 5281–5295.
- Buhl, D., Welch, W.J., Rea, D.G., 1968b. Anomalous cooling of a cratered lunar surface. *J. Geophys. Res.* 73 (24), 7593–7608.
- Chandos, R.J., Chandos, R.E., 1974. Radiometric properties of isothermal, diffuse wall cavity sources. *Appl. Opt.* 13 (9), 2142–2152.
- Colwell, J.E., Jakosky, B.M., 1987. The evolution of topography on a comet. *Icarus* 72, 128–134.
- Colwell, J.E., Jakosky, B.M., Sandor, B.J., Stern, S.A., 1990. The evolution of topography on comets. II. Icy craters and trenches. *Icarus* 85, 205–215.
- Cord, A.M., Pinet, P.C., Daydou, Y., Chevrel, S.D., 2003. Planetary regolith surface analogs: Optimized determination of Hapke parameters using multi-angular spectro-imaging laboratory data. *Icarus* 165, 414–427.
- Davidsson, B.J.R., Gutiérrez, P.J., Rickman, H., 2009. Physical properties of morphological units on Comet 9P/Tempel 1 derived from near-IR Deep Impactspectra. *Icarus* 201, 335–357.
- Davidsson, B.J.R., Gutiérrez, P.J., Groussin, O., A'Hearn, T.F.M.F., Feaga, L.M., Kelley, M.S., Klaasen, K.P., Merlin, F., Protopapa, S., Rickman, H., Sunshine, J.M., Thomas, P.C., 2013. Thermal inertia and surface roughness of Comet 9P/Tempel 1. *Icarus* 224, 154–171.
- Davidsson, B.J.R., Rickman, H., Bandfield, J.L., Groussin, O., Gutiérrez, P.J., Wilska, M., Capria, M.T., Emery, J.P., Helbert, J., Jorda, L., Maturilli, A., Mueller, T.G., 2014. The effect of roughness for spatially resolved atmosphereless bodies. *Icarus* (submitted for publication).
- Delbò, M., Tanga, P., 2009. Thermal inertia of Main Belt Asteroids smaller than 100 km from IRAS data. *Planet. Space Sci.* 57, 259–265.
- Delbò, M., dell'Oro, A., Harris, A.W., Mottola, S., Mueller, M., 2007. Thermal inertia of near-Earth asteroids and implications for the magnitude of the Yarkovsky effect. *Icarus* 190, 236–249.
- Emery, J.P., Sprague, A.L., Witteborn, F.C., Colwell, J.E., Kozłowski, R.W.H., Wooden, D.H., 1998. Mercury: Thermal modeling and mid-infrared (5–12  $\mu\text{m}$ ) observations. *Icarus* 136, 104–123.
- Giese, B., Kürt, E., 1990. Theoretical interpretation of infrared measurements at Deimos in the framework of crater radiation. *Icarus* 88, 372–379.
- Greenberg, J.M., 1986. Predicting that comet Halley is dark. *Nature* 321, 385.
- Gutiérrez, P.J., Ortiz, J.L., Rodrigo, R., López-Moreno, J.J., 2001. Effects of irregular shape and topography in thermophysical models of heterogeneous cometary nuclei. *Astron. Astrophys.* 374, 326–336.
- Hansen, O.L., 1977. An explication of the radiometric method for size and albedo determination. *Icarus* 31, 456–482.
- Hapke, B., 1984. Bidirectional reflectance spectroscopy. 3. Correction for macroscopic roughness. *Icarus* 59, 41–59.
- Hapke, B., 1996a. A model of radiative and conductive energy transfer in planetary regoliths. *J. Geophys. Res.* 101 (E7), 16817–16831.
- Hapke, B., 1996b. Application of an energy transfer model to three problems in planetary regoliths: The solid-state greenhouse, thermal beaming, and emittance spectra. *J. Geophys. Res.* 101 (E7), 16833–16840.
- Harris, A.W., Mueller, M., Delbò, M., Bus, S.J., 2005. The surface properties of small asteroids: Peculiar Betulia – A case study. *Icarus* 179, 95–108.
- Helfenstein, P., Shepard, M.K., 1999. Submillimeter-scale topography of the lunar regolith. *Icarus* 141, 107–131.
- Horai, K.-I., 1971. Thermal conductivity of rock-forming minerals. *J. Geophys. Res.* 76 (5), 1278–1308.
- Jämsä, S., Peltoniemi, J.L., Lumme, K., 1993. Thermal emission from a rough surface: Ray optics approach. *Astron. Astrophys.* 271, 319–325.
- Kürt, E., Giese, B., Keller, H.U., Ksanfomaliti, L.V., 1992. Interpretation of the KRFM-infrared measurements of Phobos. *Icarus* 96, 213–218.
- Lagerros, J.S.V., 1996. Thermal physics of asteroids. I. Effects of shape, heat conduction and beaming. *Astron. Astrophys.* 310, 1011–1020.
- Lagerros, J.S.V., 1997. Thermal physics of asteroids. III. Irregular shapes and albedo variations. *Astron. Astrophys.* 325, 1226–1236.
- Lagerros, J.S.V., 1998. Thermal physics of asteroids. IV. Thermal infrared beaming. *Astron. Astrophys.* 332, 1123–1132.
- Mueller, M., 2007. Surface Properties of Asteroids from Mid-infrared Observations and Thermophysical Modeling. PhD Thesis, Universitätsbibliothek der Freien Universität Berlin, Berlin. <[http://www.diss.fu-berlin.de/diss/receive/FUDISS\\_thesis\\_000000002596](http://www.diss.fu-berlin.de/diss/receive/FUDISS_thesis_000000002596)>.
- Müller, T.G., Blommaert, J.A.D.L., 2004. 65 Cybele in the thermal infrared: Multiple observations and thermophysical analysis. *Astron. Astrophys.* 418, 347–356.
- Özişik, M.N., 1985. Heat Transfer. A Basic Approach. McGraw-Hill, Inc., New York.
- Pettit, E., Nicholson, S.B., 1930. Lunar radiation and temperatures. *Astrophys. J.* 71, 102–135.
- Robie, R.A., Hemingway, B.S., Takei, H., 1982. Heat capacities and entropies of  $\text{Mg}_2\text{SiO}_4$ ,  $\text{Mn}_2\text{SiO}_4$ , and  $\text{Co}_2\text{SiO}_4$  between 5 and 380 K. *Am. Mineral.* 67, 470–482.
- Rozitis, B., Green, S.F., 2011. Directional characteristics of thermal-infrared beaming from atmosphereless planetary surfaces – A new thermophysical model. *Mon. Not. R. Astron. Soc.* 415, 2042–2062.
- Saari, J.M., Shorthill, R.W., 1963. Isotherms of crater regions on the illuminated and eclipsed Moon. *Icarus* 2, 115–136.
- Spencer, J.R., 1990. A rough-surface thermophysical model for airless planets. *Icarus* 83, 27–38.
- Stansberry, J.A. et al., 2012. Physical properties of trans-neptunian binaries (120347) Salacia–Actaea and (42355) Typhon–Echidna. *Icarus* 219, 676–688.